学位論文

3D Reconstruction of Typhoon and Isolated Cumulonimbus Clouds Using Satellite, Airborne and Ground Cameras

(衛星、航空機および地上での撮像に基づく台風と積乱雲の 3 次元構造推定)

by

MERYL REGINE LLENARESAS ALGODON

メリル　レジーン　レナレサス　アルゴドン

北海道大学

Supervisor: Prof. Yukihiro Takahashi

A dissertation submitted in partial fulfillment of
the requirements for the degree of Doctor of Philosophy
in the Graduate School of Science, Hokkaido University
Sapporo, Hokkaido, Japan

March 2022

Abstract

Typhoons and torrential rain are weather phenomena that inflict damages and casualties, especially in the heavily populated East and South-east Asian countries. Because of this, measuring their intensity accurately can help mitigate the hazards that they bring. However, typhoon analysis (size, shape of clouds and development rate) is difficult to perform because of its chaotic behavior and environmental factors that affect it. According to studies, the essential parameters to estimate typhoon intensity from remote sensing are cloud morphology, cloud-top height, and cloud profiling information across the center of the storm. For stronger typhoons, the typhoon eye and eyewall are also more prominent, making them good indicators of typhoon intensity. In addition, typhoons and cumulonimbus clouds that could cause torrential rains have different spatial and temporal scales. This discrepancy in scaling makes it difficult to analyze clouds using a single imaging source. Thermal infrared from meteorological satellites that measures cloud altitude are unreliable because of inconsistent atmospheric temperatures. Furthermore, radar sensors have insufficient spatial and temporal resolution to measure small cloud particles. These show that the current methods have limitations.

In this research, a method was developed to analyze typhoons and isolated cumulonimbus clouds using stereo-photogrammetry from different imaging sources. We reconstructed a precise three-dimensional model of a typhoon (Typhoon Maysak, September 2020) and a typhoon eye (Typhoon Trami, September 2018) using stereo-photogrammetry of a satellite (Diwata-2) and aircraft images respectively. The result of the stereo-photogrammetric model from satellite images has 1.17 km/pix resolution with 2.64 pix projection error while the result from aircraft images has 6.08 m/pix resolution with 2.37 pix projection error. Multiple isolated cumulonimbus clouds were also modeled through stereo-photogrammetry of images from multiple ground cameras. The resulting 3D cloud resolution from ground observation at Edogawa City last August 14, 2019 has resolution of 1.85m/pix with 4.34 pix projection error. Another observation was conducted at the same location on September 5, 2020 and the resulting 3D model has resolution of 4.5m/pix with 3.2 pix projection error. Our method has significantly higher resolution since most satellites and sensors have spatial resolution of 1 km at best, with the exception of Advanced Spaceborne Thermal Emission and Reflection Radiometer (ASTER) and Diwata-1.

For each stereo-photogrammetric model, cloud-top altitude was also estimated, and was compared with the cloud-top altitude estimated from Himawari thermal infrared (TIR) and dropsonde data. The resulting altitude from stereo-photogrammetry shows that the cloud-top altitude of Typhoon Trami has approximately 14 km altitude and has a huge overlap with the altitude estimate from TIR. However, cloud-top altitude of

Typhoon Maysak has erroneous estimate due to large camera rotation angles of Diwata-2 that were not incorporated in the 3D reconstruction. The isolated clouds from the 2019 and 2020 observations at Edogawa City have cloud-top altitudes of 6.2 km and 3.4 km respectively. Both are approximately 2 km higher than their TIR-method cloud estimates. Since ground observations are conducted at Tokyo Bay coastline, the estimate difference is attributed to the effect of surface emissivity that might have contaminated the TIR data. The altitude profile of the models has good details of the cloud structures. Finally, this study suggests the idea of analyzing clouds in volumetric perspective and could help improve the accuracy of extreme weather prediction in the future.

Acknowledgment

I would like to express my gratitude to the faculty who are involved in my study. First and foremost, to my supervisor Prof. Yukihiro Takahashi for taking me as a student and giving me an opportunity to work on this ground-breaking research. I would also like to thank Assoc. Prof. Hisayuki Kubota for guiding me along the meteorological part of my research. Thank you, Prof. Takahashi and Assoc. Prof. Kubota, for your constant patience and guidance as I navigate through my PhD. I would also like to thank Prof. Mitsuteru Sato and Assoc. Prof. Junichi Kurihara for reviewing my thesis and giving me insights beyond my way of thinking.

I would also like to thank all the people involved in my experiments in Tokyo (especially to Masataka Imai and Shigeru Fujita) and Sapporo. I would like to thank Dr. Masashi Kamogawa for helping me with my Tokyo observations and for assisting me with my research involving Mt. Fuji research station's MORECA camera. Special thanks to Ma'am Eriko Momota, Dr. Begzee Tumendemberel, Dr. Ahmad Shaqeer Mohamed Thaheer, Ohno Tatsuhara, Ryuto Hashiba and Garid Zorigoo for the guidance and resources they have given me that helped me in my study. I would like to thank Dr. Takeshi Maesaka, Dr. Tadayasu Ohigashi, Dr. Namiko Sakurai from National Research Institute for Earth Science and Disaster Resilience (NIED) for providing some of the data used in this research.

To my labmates and to all my friends who've I met here in Hokkaido, thank you so much for accompanying me throughout my PhD and making it way more fun. I could not imagine my life here in Japan without you.

I would also like to thank Dr. Joseph Joel Marciano who encouraged and supported me into taking this opportunity to study in Japan. I would like to thank my mentor, Dr. Maricor Soriano, for teaching me the fundamentals of image processing. I would like to thank SATREPS/ULAT project (SATREPS: Science and Technology Research Partnership for Sustainable Development, ULAT: Understanding Lightning and Thunderstorm) and JICA (Japan International Cooperation Agency) for providing me the resources to do my PhD here in Japan.

I would like to thank my parents, Merjelina Algodon and Regidor Algodon, and my family for their unconditional love and support. Thank you to my friends for giving me the strength to finish my PhD here in Japan. Special thanks to Adrian Chester Balingit for his constant support, emotionally and academically, during my every difficult time here in Japan. I would not be able to make it without you all.

Finally and most importantly, I would like to express my deepest gratitude towards God for giving me my life and the strength to do the things that I do. I owe everything to you.

Thank you!

Table of Contents

List of Figures

List of Tables

List of Abbreviations

ASTER	Advanced Spaceborne Thermal Emission and Reflection Radiometer
ATSR	Along Track Scanning Radiometer
BT	Brightness Temperature
dBZ	Decibel relative to Z of radar
DEM	Digital Elevation Map
DOST-ASTI	Department of Science and Technology – Advances Science and Technology Institute
ERC	Enhanced Resolution Camera
FoV	Field of View
GEOS	Geostationary Operational Environmental Satellite system
GMS	Geostationary Meteorological Satellites
HPT	High Precision Telescope
JMA	Japan Meteorological Agency
JST	Japan Standard Time
LCTF	Liquid Crystal Tunable Filter
MFC	Middle Field Camera
MISR	Multi-angle Imaging SpectroRadiometer
MODIS	Moderate Resolution Imaging Spectroradiometer
RISESAT	Rapid International Scientific Experiment Satellite
RMS	Root Mean Square
SATREPS	Science and Technology Research Partnership for Sustainable Development
SMI	Spaceborne Multispectral Imager
TIR	Thermal Infrared
T-PARCII	Tropical cyclones-Pacific Asian Research Campaign for Improvement of Intensity estimations/forecasts
ULAT	Understanding Lightning and Thunderstorm
UTC	Coordinated Universal Time
WFC	Wide Field Camera

Chapter 1

Introduction

This chapter contextualizes the research by providing background information on the importance of accurate measurement of typhoon intensity in hazard mitigation. The effects of the changing climate and how it affects the accuracy of the current weather forecasting is also discussed. Review of the current studies regarding the use of remote sensing, specifically 2D satellite imagery, for typhoon forecasting is also presented. The chapter highlights the research motivation and problem statement and thoroughly defines the research's objectives and scope. Finally, the thesis outline explains the overview for each chapter.

1.1 Research Background

Typhoons can form in a basin for as much as 20 times annually and bring strong winds, flooding, landslides, and storm surges. They cause damages and fatalities especially in the heavily populated East and Southeast Asian countries (Peduzzi, et al., 2012; Pun, Lin, & Lo, 2013). Figure 1.1 shows the aftermath of Typhoon Vamco when it hit Cagayan Province in the Philippines last November 13, 2020. Villages were destroyed from the flashfloods.

Figure 1.1 (Left) Before and (Right) after image of Cagayan Province in the Philippines after Typhoon Vamco hit it last November 13, 2020. *Image credit: DATOS Facebook Page.*

Typhoon intensity is difficult to predict because of its chaotic behavior and the environmental factors that affect it such as atmospheric and oceanic conditions. These external disturbances affect its intensity, movement and structure depending on how its eye wall responds (Wang & Wu, 2004; Yamada, Nasuno, Yanase, & Satoh, 2016). They are also vulnerable to changes in initial conditions (Butt, 2021). Not only is it difficult to get input data that is accurate enough, it should also be done at regular intervals to monitor its development.

In the past three decades, it was found out that there is a global increase in intensity and intensification rate of major typhoons due to warming scenarios (Kossin, Knapp, Olander, & Velden). Typhoons that rapidly intensify are associated with the highest forecast errors (Bhatia, et al., 2019). Thus, typhoons are expected to be more dangerous in the years to come and be more difficult to predict.

Since the earliest applications of satellite observations to meteorology, typhoon monitoring has been one of its main priorities (Hasler, et al., 1998; Wu, Chou, Cheng, & Wang, 2003; Zhu, Zhang, & Weng, 2004; Bell & Montogomery, 2008; Liu, Liu, Lin , & Chao, 2010; Liu & Chan, 1999; Li, et al., 2013). Dvorak (1975 and 1984) developed a method for estimating a typhoon's intensity by analyzing its cloud morphology, specifically its curves and shapes as shown in Figure 1.2. By measuring the size of a typhoon's central cloud features and its banding features to known typhoon growth morphology patterns, its intensity can be estimated. The Dvorak technique has been the baseline for extracting the scale of typhoons, but this technique is limited to typhoons with typical growth patterns. Additionally, due to its subjectivity, its reliability is low. To overcome this limitation, many researchers have proposed algorithms that uses satellite images (Lee, Im, Cha, Park, & Sim, 2019).

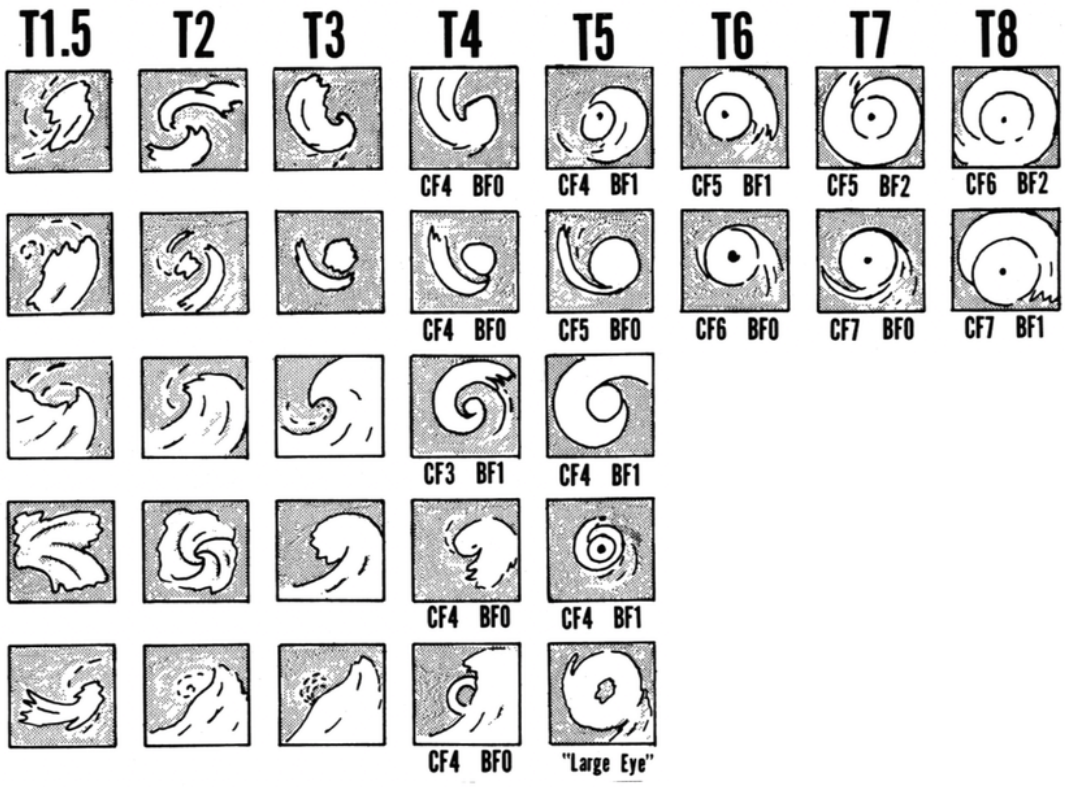

Figure 1.2 Common typhoon morphology patterns according to Dvorak. (Maskey, et al., 2020)

In the recent years, typhoon intensity estimation methods have developed to using information about the cloud-top height, cloud-top temperature, and cloud profiling across the center of the storm (Luo, et al., 2008). Several studies have also correlated typhoon intensity with the vertical cloud-top altitude movement of its eye, as well as the clarity of its eye wall boundary (Bell & Montogomery, 2008; Mack, Hasler, & Rodgers, 1983; Powell, 1990; Liu & Chan, 1999; Houze, Chen, Smull, Lee, & Bell, 2007). The stronger the typhoon, the more prominent the typhoon eye and its eyewall, making them good indicators of typhoon intensity. The typhoon eye is also an integral part in tracking and predicting the trajectory of typhoons since it is the feature being tracked. However, it could be misleading since the eye location varies with altitude due to wind shear (Cheng, Huang, Liu, Ho, & Kuo, 2012; Pan, Liu, He, Yang, & He, 2013; Jin, Wang, & Li, 2014). These imply that the observation of the eye wall in a developing typhoon is important in improving the accuracy of its intensity estimation and trajectory prediction.

One way of measuring cloud-top altitude profile is by stereoscopy. However, this prove to be challenging as cloud features required for stereo-matching might not be visible and rigid due to cloud advection and its changing morphology. Most stereoscopic techniques use multiple geostationary satellites that capture target clouds at different viewing angles (Figure 1.3) such as Geostationary Meteorological Satellites (GMS) (Takashima, Takayama, Matsuura, & Naito, 1982), Geostationary Operational Environmental Satellite system (GEOS) (Mack, Hasler, & Rodgers, 1983) and METEOSAT (Seiz, Tjemkes, & Watts, Multiview Cloud-Top Height and Wind Retrieval with Photogrammetric Methods: Application to Meteosat-8 HRV Observations, 2007). The accuracy of these techniques is dependent on the acquisition-time difference between two satellites since their capture time are not usually synchronized. Conversely, there are stereoscopic systems that utilize a single satellite that have multiple cameras to capture multi-view angles of the clouds such as Along Track Scanning Radiometer (ATSR) (Prata, 1997; Naud, et al., 2007), Multi-angle Imaging Spectro Radiometer (MISR) (Moroney, Davies, & Muller, 2002; Seiz, Davies, & Grun, Stereo cloud-top height retrieval with ASTER and MISR, 2006), Moderate Resolution Imaging Spectroradiometer (MODIS), Advanced Spaceborne Thermal Emission and Reflection Radiometer (ASTER) (Seiz, Davies, & Grun, Stereo cloud-top height retrieval with ASTER and MISR, 2006) and the Philippines' microsatellite DIWATA-1 (Castro, et al., 2020). These setups have the advantage for near-simultaneous capture, but none guarantees high temporal resolution data. Most satellites take around 2.5 mins to 7.5 mins between captures, with the exception of DIWATA-1 with 200ms temporal resolution.

In 1991, the earliest technique for reconstructing three-dimensional models of typhoons was used to estimate cloud-top height (Hasler, Strong, Woodward, & Pierce, 1991). However, they utilized synthetic stereo matching to approximate the probable cloud structure with a 1.5 km vertical resolution which is low for cloud-top height estimation. A laboratory from (National Aeronautics and Space Administration (NASA), Jet Propulsion Laboratory (JPL), used Terra MISR to reconstruct a 3D model of Tropical storm Laura. Terra MISR has a highly specialized imaging payload for the 3D reconstruction. Their method cannot be utilized using existing satellites with standard imaging payload (National Aeronautics and Space Administration (NASA), 2020).

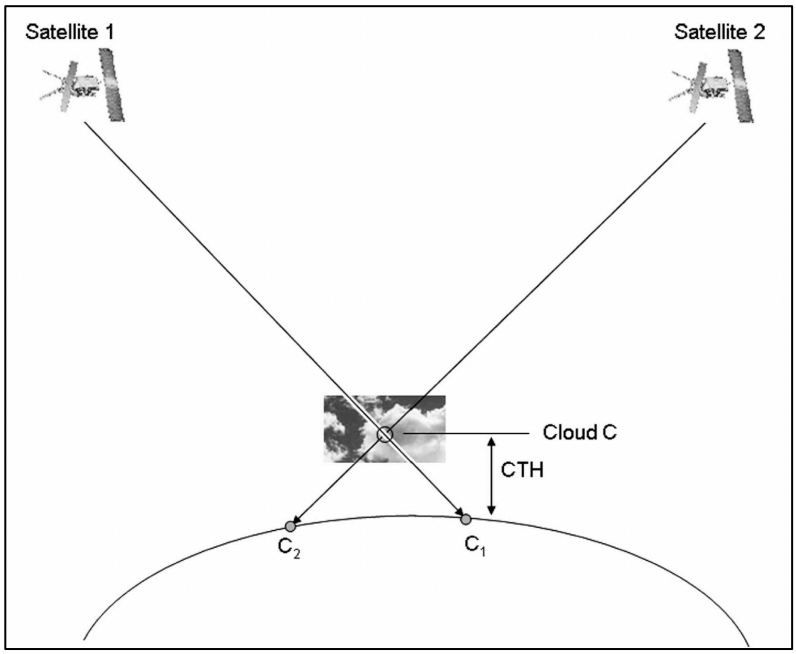

Figure 1.3 Stereoscopy using multiple geo-stationary satellites to capture images of a target cloud at different viewing angles (Seiz, 2007)

1.2 Research Motivation & Problem Statement

There is increasing demand for accurate typhoon forecasting as extreme weather will continually get more dangerous and more difficult to predict in the future. Methods were developed for estimating a typhoon's intensity based on its morphology, cloud altitude, and altitude profile, that can be measured from satellite images and other remote sensing data. Currently, we have an abundance of 2D satellite images to monitor typhoons but knowing what they look like is not sufficient to understand their intensity. This implies that typhoons should be analyzed in a volumetric perspective to help extract more information.

Stereoscopy was then used to estimate cloud-top altitude from multiples images of a target cloud at different viewing angles. However, having these images does not guarantee that a 3D model can be reconstructed from them since the temporal resolution and the distance between the capture locations are crucial for stereo-matching of cloud features.

Another concern is that a typhoon is not the only weather event that could cause torrential (heavy) rain, it could also be due to the presence of a cumulonimbus cloud. Both spatially and temporally, torrential rain from cumulonimbus clouds can be very difficult to predict. Generally, it takes place on a small spatial scale with less than 100 km and over a short time span of less than 12 hours (Schumacher, 2017). In comparison, most typhoons have sizes ranging from 200 to 500 km but a few can reach up to 1000 km (World Meteorological Organization, 2021). They can rapidly intensify into Category 5 typhoons within 24 hours and can last from a day, up to a month.

There is also a rising concern with the prevalence of these events, which many scientists link to climate change (Hayhoe, et al., 2018). Because of this, a method for observing torrential rains at different spatial and temporal scales should be devised.

1.3 Research Objectives

This research aimed to:

i. develop a better understanding of the meteorological events that cause torrential rain (typhoons and cumulonimbus clouds) with properties such as intensity and amount of precipitation,
ii. develop an approach for analyzing typhoons and cumulonimbus clouds by utilizing stereo-photogrammetry and multiple imaging sources,
iii. use stereo-photogrammetry to reconstruct a precise 3D model of a typhoon and typhoon eye using Diwata-2 and aircraft images,
iv. reconstruct cumulonimbus clouds using ground camera images,
v. analyze the information that can be extracted from stereo-photogrammetric models of cumulonimbus clouds and typhoons such as the cloud-top height and the cloud profile and compare them to the cloud-top height estimated using brightness temperature (BT) from Himawari-8 thermal infrared (TIR) band,
vi. predict typhoon intensity and the amount of rainfall from typhoons and cumulonimbus clouds from volumetric analysis of clouds.

1.4 Research Scope

The extent of this study is divided into how stereo-photogrammetry is applied on three different imaging sources: satellite images, aircraft images and ground camera images. For each method, a total of six field observations were conducted and presented in this research – one from satellite observation, one from aircraft typhoon reconnaissance, and 4 from ground observations. In general, the observations were for obtaining the stereo-images that will then be reconstructed into 3D models for further altitude profile analysis. However, it is beyond the study's scope to estimate the typhoon intensity from the research output.

The satellite observations and aircraft reconnaissance were used to observe Typhoon Trami (2018, September 26) and Typhoon Maysak (2020, September 2) respectively, both at southern Japan near the Pacific region. As for the field ground measurements, the chosen location is Kasai Rinkai Park in Edogawa City where 2019 and 2020 ground camera campaigns were conducted. This park has a wide-open area facing the Tokyo Bay where there is a good view of incoming clouds, ideal for the multiple ground camera setup. The two remaining ground campaigns were conducted at different locations. The first is located at Yoyogi Park in Shibuya City and the second is located within Hokkaido University in Sapporo City. Both locations were selected based on the field of view of Diwata-2 and RISESAT (Rapid International Scientific Experiment Satellite) during the time of capture. Lastly, the measurement is done during Japan's typhoon season (July-October), which has high cloud density to increase the chances of cumulonimbus cloud observation. Due to weather limitations, only the ground campaigns conducted at the Kasai Rinkai Park will be presented in the results.

1.5 Thesis Outline

The overall structure of the study is separated by the analysis of the three stereo-photogrammetry techniques. After the introduction in this chapter, Chapter 2 presents the different instrumentation utilized in the research – satellites, cameras, and aircraft.

Chapter 3 begins by outlining the chapter's overview, and subsequently describes all the field experiment that is covered in this research. It discusses the meteorological events and experimental approach during the experiments. In Chapter 4, the scientific framework behind stereo-photogrammetry and the methods used in this research will be explained, including the standard methods of using the satellite's thermal infrared in estimating the cloud-top altitude. Afterward, Chapter 5 will present the result of the stereo-photogrammetry and its estimated cloud-top altitudes for each campaign. This will include the comparison between stereo-photogrammetry and the use of satellite's TIR in estimating the cloud-top altitude.

Chapter 6 discusses the significant findings for each experimental work and how it is interpreted in a meteorological perspective. It also highlights the research's unique characteristics, as well as the limitations of this research.

Finally, Chapter 7 summarizes the main findings of this research and its conclusion. The chapter gives an insight into other possible points of future work.

Chapter 2

Instruments

This chapter aims to introduce the various instruments used in this research.

2.1 Satellite

There were two satellites utilized in this research: Diwata-2 and Himawari-8. Diwata-2 was used to capture panchromatic images of Typhoon Maysak. On the other hand, the images from Himawari-8 were used to geo-reference the resulting 3D model from all observations. Himawari-8's TIR was also used to estimate cloud-top altitude.

2.1.1 Diwata-2

DIWATA-2 is microsatellite built by Filipino students in the Philippine Microsat (PHL- MICROSAT) Program in collaboration with Hokkaido University and Tohoku University. Its dimension is $50cm \times 50cm \times 50cm$ with an estimated mass of 56 kg as seen in Figure 2.1. It was launched into an orbital altitude of 595 km × 616 km, 97.84° from the Tanegashima Space Center in Japan via the H-II F40 rocket on October 29, 2018 (UP Media and Public Relations Office, 2018). Diwata-2 carries the five optical payloads to support its mission objective of observing cloud patterns and weather disturbances.

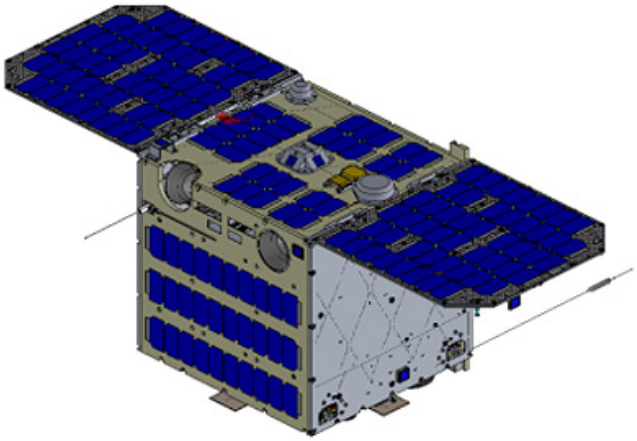

Figure 2.1 Image of Diwata-2. *Image credit: Phl Microsat*

DIWATA-2's payloads are: a high-precision telescope (HPT) and wide-field camera (WFC); a space-borne multispectral imager (SMI) with Liquid Crystal Tunable Filter (LCTF); a middle-field camera (MFC); and an Enhance Resolution Camera

(ERC) which is an addition from its earlier version. All images except from the ERC have a dimension of 659 pixels by 494 pixels. In this study, the ERC is a panchromatic camera that was selected for its advantageous image resolution of 1688 pixels by 1248 pixels (2.1 MPx). The ERC has spatial resolution of 54.6 m.

The DIWATA-2 target-pointing capability was also utilized in this study; this allows the microsatellite to point and lock the cameras to view a specific location as it moves through its orbit. Stereoscopy-based measurement of cloud-top heights can be performed with multiple cameras in a steady position, as in the case of geosynchronous satellites. In the case of Diwata-2, only ERC was used as it is the only camera with enough spatial and temporal resolution to capture images of typhoons at different locations within a short time frame. It can capture 10 images of the subject per observation at 500ms at an orbital speed of 7.5 km/s. This results to multiple images of the typhoon captured at different locations at approximately the same time.

Diwata-2 is a sun-synchronous satellite and once its target is out of its field of view (FoV), it will need to take another 24 hours to conduct another observation of the same target. Another disadvantage is that depending on the location and distance of the target, the camera may have large rotation angle relative to its target and could cause difficulty in the 3D reconstruction.

2.1.2 Himawari-8

HIMAWARI-8, a Japanese geo-stationary weather satellite, captures multi-spectral images of the Asia-Pacific region every 10 minutes. At an altitude of approximately 35,000 km, it covers the latitude ranging from 60N to 60S and longitude from 85E to 205E (155W). It has 16 spectral bands that comprises of 4 visible bands, 2 short-infrared bands and 10 thermal infrared bands (Meteorological Satellite Center of Japan Meteorological Agency, 2021). The red visible band (0.64 μm) of HIMAWARI-8 has the highest image resolution of 24000 pixels by 24000 pixels (576 Mpx) and spatial resolution of 500m. The image quality from this band is enough to identify large cloud features present and was used to geo-reference the output 3D models.

For the cloud-top estimation technique, the thermal infrared band (10.4 μm) was used since the cloud radiance is within the 3.7 μm to 11 μm infrared range (Menzel, 2004). This band has an image resolution of 6000 pixels by 6000 pixels and spatial resolution of 2 km.

2.2 Aircraft

SATREPS/ULAT (SATREPS: Science and Technology Research Partnership for Sustainable Development, ULAT: Understanding Lightning and Thunderstorm) is a collaborative project of Hokkaido University, Tokyo Metropolitan University, Department of Science and Technology - Advanced Science and Technology Institute (DOST-ASTI) and University of the Philippines Diliman (Department of Science and Technology - Advanced Science and Technology Institute, 2016). One of its objectives is to improve extreme weather monitoring by creating 3D models of thunderclouds using meteorological satellites (Castro, et al., 2020). Another project from Nagoya University, titled “Tropical Cyclones - Pacific Asian Research Campaign for Improvement of Intensity estimations/forecasts” (T-PARCII), conducts typhoon

monitoring using multiple sensors deployable from an aircraft such as dropsonde, balloons, and radar (Tsuboki, 2017).

T-PARCII conducts aircraft reconnaissance to monitor the inner core of typhoons with the objective of improving the accuracy of typhoon forecasting. During these reconnaissance, multiple dropsondes developed by Meisei Electric Co., LTD. and Nagoya University were deployed from the top of typhoons (Ito, et al., 2018). These dropsondes measures pressure, humidity, temperature, wind direction/speed, and three dimensional GPS position at 1 Hz frequency (Yamada, et al., 2021).

In this research, SATREPS/ULAT partnered with T-PARCII to conduct an experiment that captures multiple images of Typhoon Trami from an aircraft (Figure 2.2) to get high-resolution images of the typhoon eye. The aircraft "Diamond Air Service" traversed the typhoon's eye and eyewall at the mean elevation of 13.66 km and at the speed of 200m/s. This data from the reconnaissance has significantly higher resolution than most geostationary satellites, ensuring that the fine cloud features are visible. The aerial photographs used in this study have pixel resolution of approximately 6.08 m which have significantly higher spatial resolution than most satellites (Mack, Hasler, & Rodgers, 1983; Seiz, Tjemkes, & Watts, Multiview Cloud-Top Height and Wind Retrieval with Photogrammetric Methods: Application to Meteosat-8 HRV Observations, 2007; Prata, 1997; Moroney, Davies, & Muller, 2002; Seiz, Davies, & Grun, Stereo cloud-top height retrieval with ASTER and MISR, 2006; Genkova, Seiz, Zuidema, Zhao, & Di Girolamo, 2007).

Figure 2.2 Aircraft used during the September 26, 2018 recconnaisance to capture images of Typhoon Trami eye. *Image credit: Hisayuki Kubota.*

The camera used for the experiment is a Nikon D5500 camera with a focal length of 18mm, an aperture diameter of 14mm, and an exposure time of 1.25ms. The image resolution is 6000 pixels by 4000 pixels, taken at intervals of 2 seconds. The exact camera pose is unknown, and this could cause erroneous orientation on the 3D output. However, camera rotation can be estimated based on knowledge of the horizon as seen on the images.

For this stereo-photogrammetry technique, it is possible to increase the image resolution and temporal resolution depending on what camera and settings were used. This makes it ideal for stereo-photogrammetric measurements of the cloud-top altitude as it decreases the errors caused by cloud advection and their changing morphology.

2.3 Ground Camera

For the ground campaign, five cameras 200m apart were used, each located 200m apart. This distance is based on the ideal viewing angle for the 3D imaging software to work. Through trial and error, it was discovered that the angle between two adjacent ground cameras relative to the target cloud should not be more than 10 degrees, assuming that the distance of the target cloud is approximately 3 km or less. This ensures that each camera is seeing a different view angle but still have large enough feature overlaps with each other. The cameras should ideally be located at a vast open area with direct view of the sky.

The camera used for this experiment is a Sony $\alpha 6400$ (Figure 2.3) with image resolution of 6000 pixels by 4000 pixels (24 MPx). The focal length is set to 16mm, the aperture is set to F22 (the camera's largest setting), the ISO is set to 200, and the exposure is set to "Averaging" so the camera automatically changes exposure depending on the moving target. The cameras are synchronized to automatically capture images at a 30s interval. This will ensure that the cameras are capturing cloud images at the same time so the error from cloud advection and changing morphology is minimized.

Figure 2.3 Camera setup for the ground campaign.

Among all the techniques presented in this research (using satellite, aircraft, and ground images), the use of multiple ground cameras for stereo-photogrammetry is the most cost-efficient and easiest to use for isolated clouds. It has a spatial resolution of approximately 1.85m to 4.5m, depending on the distance of the target clouds to the cameras. This spatial resolution is the highest among the three methods. Because of these advantages, this approach should be utilized more by constructing a semi-permanent setup of multiple cameras located at different high elevations.

Ground Camera Setup

Among the stereo-photogrammetric imaging sources, the ground cameras have the advantage of being the most cost-effective and easiest to use without compromising the image resolution. However, this technique is opportunistic and requires good atmospheric conditions and cloud position. To increase the chances of getting good data, the camera locations should be elevated to minimize the obstruction of cameras' FoV. There should also be a good amount of image overlap between adjacent cameras.

The amount of image overlap will be discussed in detail in a subsection of Chapter 4.1. In addition, the time scale for image capture should not be limited by the camera's battery capacity.

To address this issue, a camera setup was developed where the capture time is synchronized using a GPS module and Arduino Nano. The GPS module detects the time at a millisecond resolution and the Arduino Nano triggers the camera capture every 30th second of the minute. The circuit diagram of the model is shown in Figure 2.4. A Sony multiport connector pinout was connected to the camera where different pins trigger different camera actions as summarized in Table 2.1.

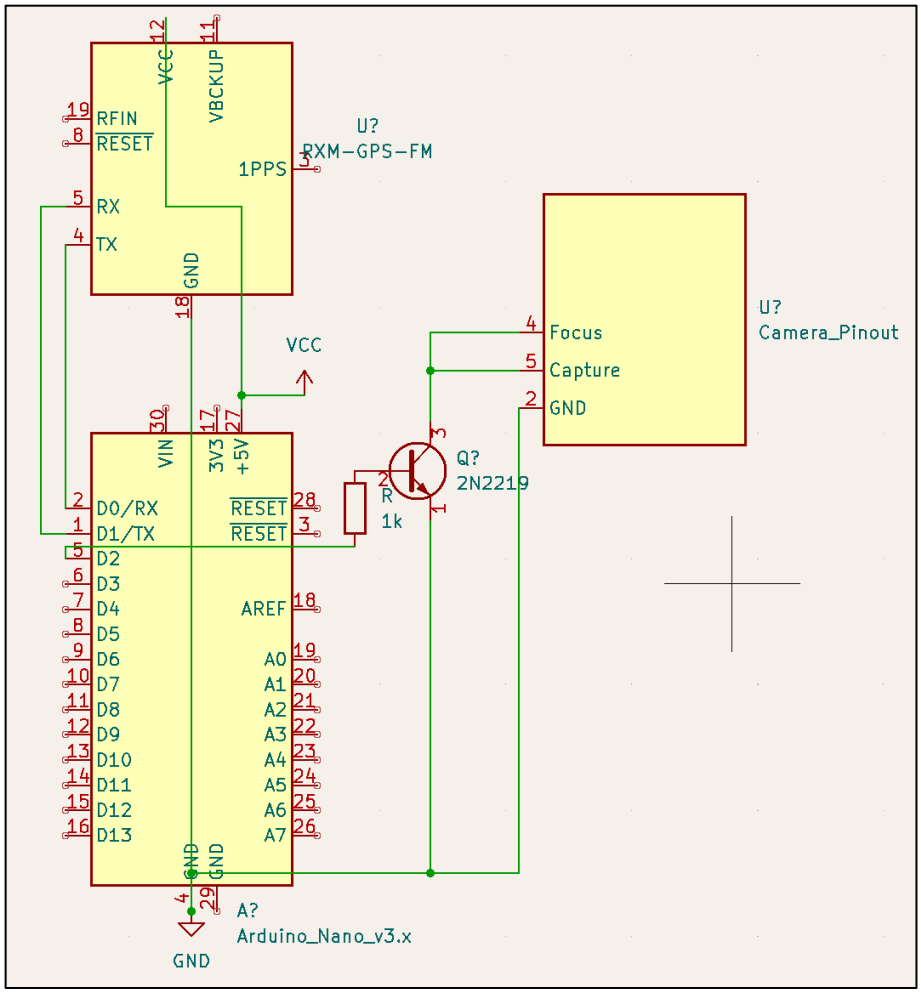

Figure 2.4 Circuit Diagram of the Ground Camera setup for synchronized capture time.

Table 2.1 Sony multiport connector pinout

Pin Number	Function
1	On/Off Trigger
2	Ground
4	Camera Focus
4 + 5	Capture Trigger

The circuit was implemented on a circuit board as shown in Figure 2.5 and the setup was tested to check if the camera capture time will be synchronized. During the testing, it was observed that there is a 1 to 3 second delay on the capture among the

five cameras but this delay has a negligible effect for the stereo-photogrammetric reconstruction. The setup is still in its preliminary stage and has yet to be installed semi-permanently in water-proof cases located on top of buildings. The cameras are to be powered by a solar power bank to prolong the capture time.

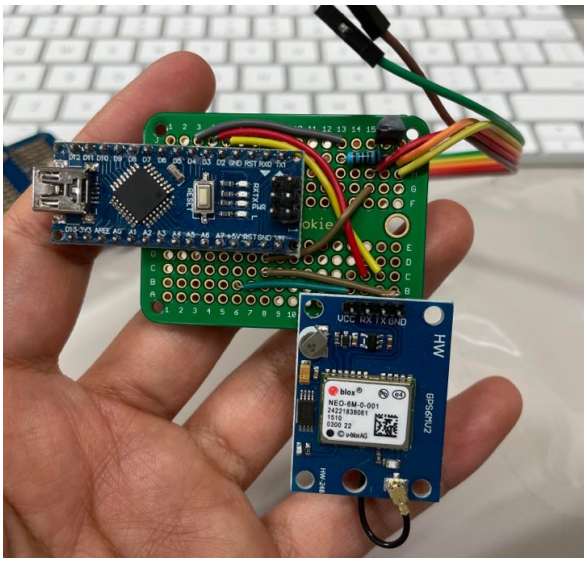

Figure 2.5 Implemented circuit for ground camera synchronized capture time.

2.4 Ka-band Radar

Five ka-band radars were deployed around the heavily populated Tokyo metropolitan area that is prone to heavy rains (Maesaka, 2015). The objective of the ka-band network is to detect the early development of cumulonimbus clouds. They are designed to respond to -13 dBZ, when rainwater is generated from the clouds based on Kessler's warm rain parametrization threshold. Because of this, the ka-band radars have sensitivity at -17 dBZ with an observation range of 20 km at 150 m range resolution.

In this research, out of the five ka-band radars, the one located in Matsudo City (MTD) was used where its latitude is at 35.76536°N and longitude is at 139.88758°E and has an altitude of 24m. It has a frequency of 34.93 GHz and a beam width of 0.31°. A pulse width of 1.0 ms (short) is used for distances less than 8.7km. On the other hand, a pulse width of 55 ms (long) is used for distances beyond 8.7 km to improve range resolution and sensitivity. MTD ka-band radar was used to validate cloud-top altitude of a target cloud that was observe in Edogawa City. Observations for elevation angles 2.2°, 6.5°, 15°, 20° are conducted every 2 minutes while observations for elevation angle 10° are conducted every 4 minutes.

The cloud-top altitude height can be estimated using the known distance of the ka-band radar to the target cloud. For all elevation angles the target cloud is present, it is assumed to be within that altitude range. This approach can help validate the altitude measured by the stereo-photogrammetric model of typhoons and isolated cumulonimbus clouds captured within the radar's observation range.

Chapter 3

Observations

This chapter describes the observations conducted for the different techniques used in this research: the Diwata-2 observation for Typhoon Maysak, the aircraft reconnaissance for Typhoon Trami, and ground campaigns for cumulonimbus cloud observations. The last section will cover all the ground observations that were conducted during the span of this research.

3.1 Satellite Observation for Typhoon Maysak

Typhoon Maysak is the ninth typhoon observed by Japan Meteorological Agency (JMA) last 2020. It developed at the east of the Philippines on August 26 and lasted for 144 hours (6 days). It has maximum sustained winds of 95 knots and reached the intensity of a Category 4 typhoon (Mainichi Japan, 2020). It hit the Kyushu region of south-western Japan last September 2, 2020. During this time, Diwata was in a good position to capture Typhoon Maysak. Ten images were captured for each of the three observations done every 1 minute. The red points on Figure 3.1 correspond to the position of Diwata-2 for each observation. The box represents the estimated FoV of the satellite's camera. The images from the first two observations produced highly saturated images and were not used in this research.

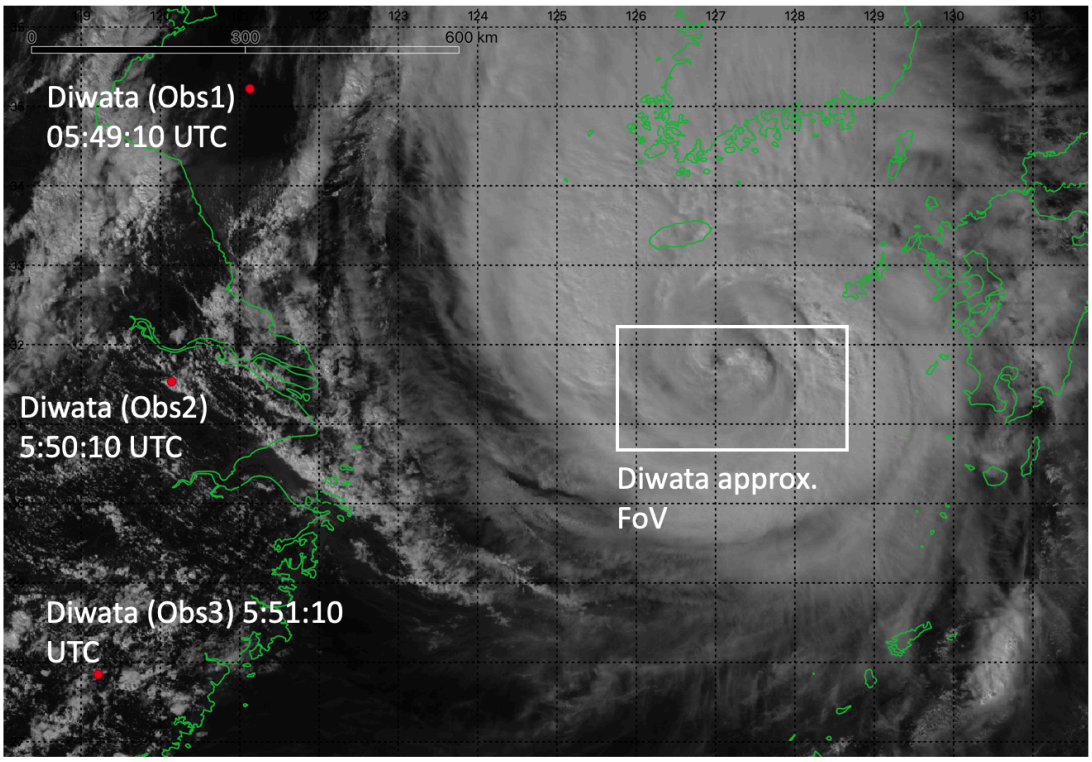

Figure 3.1 Diwata-2 locations during Typhoon Maysak observation on September 2, 2020 as seen on Band 3 (0.64 µm) of Himawari-8 (05:50:00 UTC)

During the third observation, Diwata-2 is located at 27.846º N and 119.218º E with mean altitude of 601km traversing at velocity of 7.5 km/s from 05:51:10 UTC (Coordinated Universal Time) to 05:51:15 UTC. With an estimated distance of 880 km from the typhoon's eye, the spatial resolution is at 1.17km per pixel. Since the initial and the final position of the satellite is known during the observations, the images were geotagged based on the satellite's trajectory. The satellite altitude was also incorporated to the image metadata.

3.2 Aircraft Campaign for Typhoon Trami

Typhoon Trami is a category 5 typhoon with maximum sustained winds of at least 35mph typhoon that hit Japan in September 2018 (Ornauer, 2018). It developed on September 20, 2018 at the Pacific region and moved its way north-westward. The typhoon reached its lifetime maximum intensity on September 25 and slowly decayed on the following days. In this research, we visualized Typhoon Trami's eye and eyewall structure. We also measured the cloud-top altitude through stereo-photogrammetry of images taken by a monocular camera from an aircraft.

On September 26, 2018, a T-PARCII aircraft deployed 22 dropsondes but only 18 dropsondes were observed around Typhoon Trami. The dropsonde locations were shown as orange diamonds in Figure 3.2. The aircraft also penetrated the eye of Typhoon Trami and utilized multiple images of its typhoon eye from 14:56:44 JST (Japan Standard Time) to 14:56:59 JST or 5:56:44 UTC to 5:56:59 UTC. It traversed the top of the typhoon eye at a speed of approximately 200 m/s and at a mean altitude of 13.66km from 20.85°N and 128.96°E to 20.87°N and 128.99°E. Eight consecutive images were selected for stereo-photogrammetry based on the amount of image overlap and clarity. The measurement of image overlap is explained in detail in the stereo-

photogrammetry subsection of chapter 4. The images were geotagged, and the camera altitude was coded in their metadata.

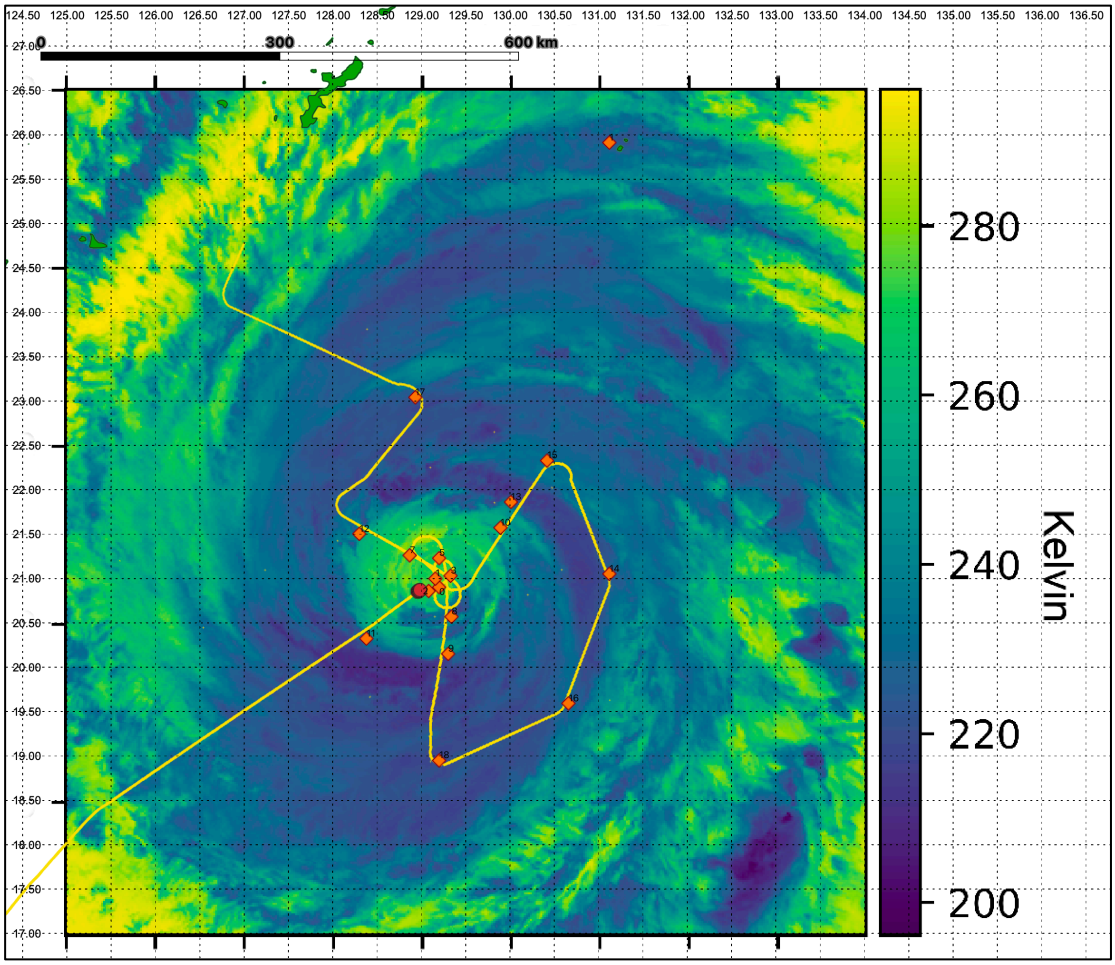

Figure 3.2 Location of the dropsonde measurements (orange diamonds) plotted on Typhoon Trami brightness temperature. The yellow line indicates the flight track and the red circles are the location of the Typhoon Trami images used for the 3D reconstruction.

3.3 Ground Campaign

In this section, all the ground observations will be presented. Since this method is an opportunistic approach to stereo-photogrammetry, success rate is highly dependent on the location and the atmospheric conditions during the time of the observation. Ground observations were conducted every typhoon season in Japan (July to October) from 2019 until 2020, whenever the density of cumulonimbus clouds is high.

3.3.1 2019 August 13-15 Tokyo Fieldwork

Last 2019, Typhoon Krosa, a category 3 typhoon, slowly developed on the Philippine sea on August 5 and moved towards southern Japan before it dissipated on August 15 (JAXA, 2020). Because of this, the first trial of the ground campaign was conducted from August 13 to August 15. On the first day of observation, regions of high precipitation probability within Tokyo prefecture were surveyed and Tachikawa City was the selected location. The five Sony α6400 cameras were positioned along the

Tama river with camera locations summarized in Table 3.1 and Table 3.2. The open area along the river offers the least obstruction of the camera FoV. For the duration of the experiment, the cameras are pointed mostly at the south-east direction of the river, where most of the cumulonimbus clouds originate from. A large cumulonimbus cloud was observed from a distance and was selected as the target cloud. However, some strato-cumulus clouds drifted and occluded the targeted cloud. The best set of images for the duration of the observation was taken around 13:33 JST as shown in Figure 3.3. The images from the five cameras were processed for stereo-photogrammetry. However, the cloud is too far from the camera location for the stereo-matching points to be identified by the 3D imaging software. Thus, the output 3D model has smooth to flat features.

Table 3.1 Camera locations for August 13, 2019 Ground Campaign at Tachikawa City (12:25 JST - 14:40 JST, Camera Direction at 119° SE - 122° SE)

	Camera 1	Camera 2	Camera 3	Camera 4	Camera 5
Latitude	35.664722	35.671111	35.668611	35.670278	35.672550
Longitude	139.431667	139.426111	139.428056	139.426667	139.4250423

Table 3.2 Camera locations for August 13, 2019 Ground Campaign at Tachikawa City (17:09 JST – 18:30 JST, Camera Direction at 316° NW)

	Camera 1	Camera 2	Camera 3	Camera 4	Camera 5
Latitude	N35°40'20"	N35°40'1"	N35°40'8"	N35° 40'13"	35.6728679
Longitude	E139°25'43"	E139°25'46"	E139°25'40"	E139°25'36"	139.4248036

Figure 3.3 Image from Camera 1 taken on August 13, 2019 at 13:33 JST.

A MORECA camera located at Mt. Fuji Research Station was used by meteorologists to monitor real-time cloud formation along its FoV (Kamogawa, 2020). It is possible to estimate the cloud-top altitude using this camera's known elevation so it can be used for validating cloud-top altitude from stereo-photogrammetry. Figure 3.4

shows the cloud formation as seen by the MORECA FoV during the time of the ground observation. However, based on the distance and location of the observation site relative to the MORECA camera, closer cloud formations were blocking the MORECA camera and therefore, the output from this day cannot be validated and will not be presented in the results.

Figure 3.4 Image captured by MORECA camera from Mt. Fuji Research Station on August 13, 2019 at 13:33:22 JST.

For the rest of the campaign period, the observation was conducted at the Kasai Rinkai Park in Edogawa City. The open area facing the Tokyo Bay is ideal for the objective of the experiment. On August 14, large isolated clouds were moving from the south-eastern part of Japan towards the north. The best set of images for the duration of the observation was taken around 14:25 JST. On August 15, there were no isolated clouds observed so the experiment was discontinued. The information for the rest of the campaign was summarized in Table 3.3 and Table 3.4.

Table 3.3 Camera locations for August 14, 2019 Ground Campaign at Edogawa City (14:11 JST – 16:00 JST, Camera Direction at 177° N - 219° N)

	Camera 1	Camera 2	Camera 3	Camera 4	Camera 5
Latitude	N35°38'22"	N35°38'19"	N35°38'21"	N35°38'20"	N35°38' 52"
Longitude	E139°51'2"	E139°51'45"	E139°52'6"	E139°52'14"	E139°50'15"

Table 3.4 Camera locations for August 15, 2019 Ground Campaign at Edogawa City (12:47 JST - 14:30 JST, Camera Direction at 280° W)

	Camera 1	Camera 2	Camera 3	Camera 4	Camera 5
Latitude	N35°38'19"	35.639084	N35°38'23"	N35°38'26"	N35°38' 52"
Longitude	E139°51'46"	139.859589	E139°51'26"	E139°51'18"	E139°50'15"

3.3.2 2020 September 5-9 Tokyo Fieldwork

The second trial for the ground camera setup was conducted from September 5 to 9. Around this time, Typhoon Haishen, a Category 2 typhoon, hit Japan on September 6. This caused a large density of cumulonimbus clouds to appear around the Edogawa region, where three out of five observation days were conducted – September 5, 6 and 8. The camera locations and experiment duration in these days were summarized in

Table 3.5 to Table 3.9. On September 5, large clusters of clouds were observed, and the set of images chosen for stereo-photogrammetry was selected at the time of 16:18 JST as seen in Figure 3.5. No data was selected on September 6 since the clouds are almost homogeneous. On September 7, the experiment was conducted at Tokyo Sky Tree in Sumida City, the tallest tower in Japan. High elevation is ideal for the objective of the experiment when conducting within the city proper as it minimizes blockage of the camera FoV. However, no data was captured this time as only a few isolated clouds can be observed from a distance. September 8 observation was conducted at Kasai Rinkai Park but the sky was clear as Typhoon Haishen was already dissipating. On September 9, the sky was clear, so no data gathering was done. However, Tokyo Tower in Minato City was visited to survey possible camera locations for the next ground campaign.

Table 3.5 Camera locations for September 5, 2020 Ground Campaign at Edogawa City (13:31 JST – 14:35 JST)

	Camera 1	Camera 2	Camera 3	Camera 4	Camera 5
Latitude	35.6419391	35.63944444	35.6387601	35.68887	35.63916667
Longitude	139.8526334	139.85777778	139.8617184	139.866366	139.87000000

Table 3.6 Camera locations for September 5, 2020 Ground Campaign at Edogawa City (15:48 JST - 16:42 JST)

	Camera 1	Camera 2	Camera 3	Camera 4	Camera 5
Latitude	35.64194444	35.63944444	35.63861111	35.638749	35.63944444
Longitude	139.85250000	139.85777778	139.86166667	139.866289	139.86944444

Table 3.7 Camera locations for September 6, 2020 Ground Campaign at Edogawa City (14:01 JST – 14:52 JST)

	Camera 1	Camera 2	Camera 3	Camera 4	Camera 5
Latitude	35.6389885	35.6394444	35.6387830	35.638901	35.6394444
Longitude	139.8608336	139.85777778	139.8617436	139.866304	139.86944444

Table 3.8 Camera locations for September 8, 2020 Ground Campaign at Edogawa City (11:36 JST - 12:09 JST)

	Camera 1	Camera 2	Camera 3	Camera 4	Camera 5
Latitude	35.6420672	35.6397315	35.6386373	35.63888889	35.63916667
Longitude	139.8525067	139.8576160	139.8620966	139.88277778	139.87000000

Table 3.9 Camera locations for September 8, 2020 Ground Campaign at Edogawa City (13:59 JST – 15:53 JST)

	Camera 1	Camera 2	Camera 3	Camera 4	Camera 5
Latitude	35.64194444	35.6397315	35.6387838	35.63888889	35.63944444
Longitude	139.85250000	139.8576160	139.8616182	139.86611111	139.86972222

Figure 3.5 Image captured by Camera 4 during the September 5, 2019 (16:18 JST) ground campaign in Edogawa City

3.3.3 2020 September 11 Sapporo Fieldwork

One of our objectives is to validate cloud-top altitude using multiple instrumentations. RISESAT is a microsatellite developed by Tohoku University in partnership with Hokkaido University and Kyoto University under the FIRST (Funding Program for World-Leading Innovative R&D on Science and Technology) program (Yoshida, et al., 2011; Kuwahara, et al., 2012; Kubo-oka T. , Kunimori, Takenaka, Fuse, & Toyoshima, 2012). On September 11, 2020 (08:36 JST), RISESAT was set to capture images of clouds on Hokkaido, Japan. Because of this, a ground campaign was conducted in an attempt to synchronize capture of RISESAT with ground cameras. The cameras were positioned around the agricultural area of Hokkaido University with exact locations listed in Table 3.10. The cumulonimbus clouds observed during the campaign were clustered and homogeneous as seen in Figure 3.6, making the data unusable for stereo-photogrammetry. However, the ground camera FoV was still verified if it is within the RISESAT FoV.

The RISESAT captured 20 images during the observation, from 23:33:22 UTC to 23:33:26 UTC, with 250ms between captures. These images were stitched to get a wider view of the cloud area. Cloud features were compared to the ones seen from Himawari-8 Band 3 (0.64 μm) to geo-reference the satellite images from RISESAT. Upon comparison, the estimated location of the ground campaign is indicated by the red point in Figure 3.8 which is outside the RISESAT FoV.

Figure 3.6 Image captured by Camera 4 during the September 11, 2020 (08:36 JST) ground campaign in Sapporo City

Table 3.10 Camera locations for September 11, 2020 Ground Campaign at Sapporo City (08:30 JST – 08:57 JST)

	Camera 1	Camera 2	Camera 3	Camera 4	Camera 5
Latitude	43.072491	43.0735978	43.0763006	43.0784535	43.084722
Longiture	141.339412	141.3380622	141.3374470	141.3338126	141.335556

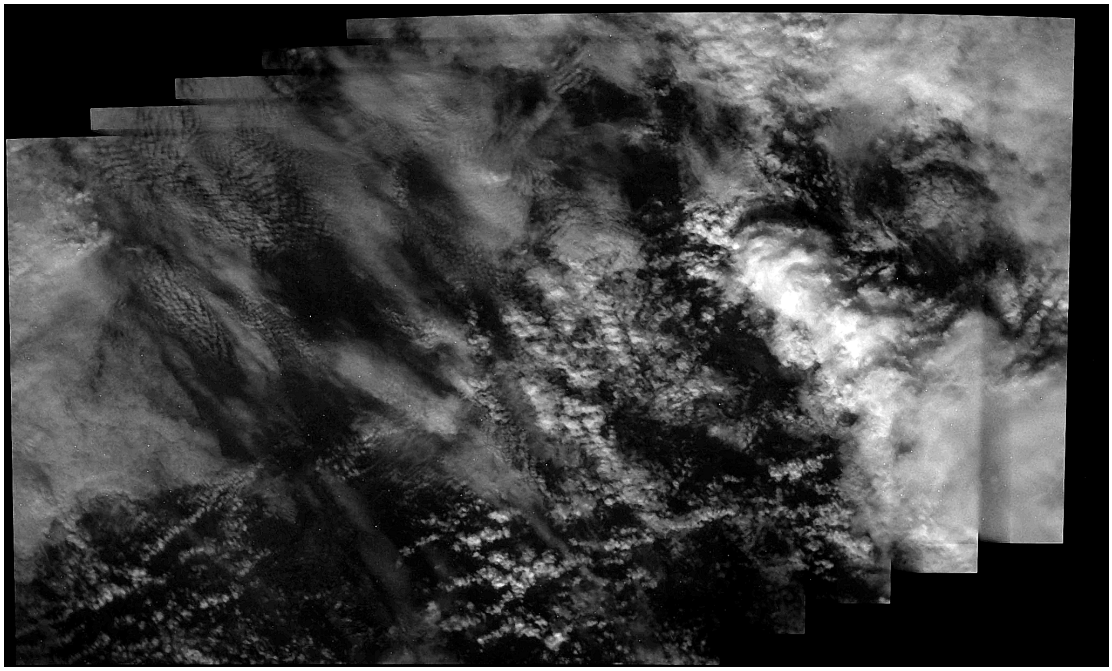

Figure 3.7 RISESAT capture on September 11, 2020 at 08:36 JST.

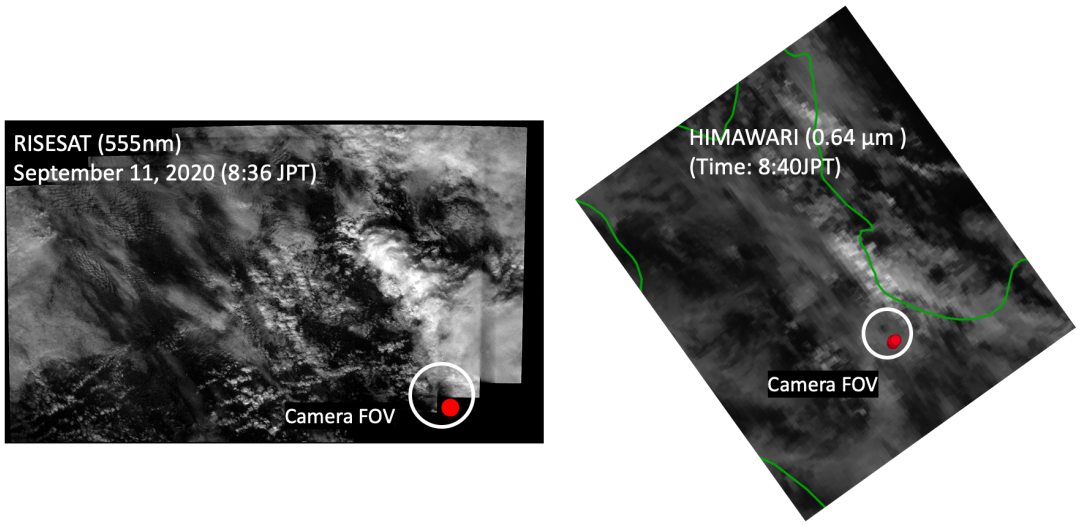

Figure 3.8 Comparison of cloud features between RISESAT and Himawari-8 captured on September 11, 2020.

3.3.4 2021 August 22-26 Yoyogi Park Fieldwork

The most recent ground campaign was conducted from August 22 to 26 at Yoyogi Park, Shibuya City. The location was designated based on the FoV of satellite observations (Diwata-2, RISESAT). However, the open area in the park was closed for the whole duration of the campaign due to 2021 Olympics event so the cameras are positioned at closer intervals of 100m-150m apart. On the last day, a larger area of the park was closed, and the camera distance was limited to 30m-70m apart. The camera locations for the duration of the ground campaign are listed in Table 3.11 to Table 3.17. This limits the FoV of the cameras and minimizes the effect of disparity (displacement in the apparent position of the feature in the image as viewed between two camera angles) that aids in 3D reconstruction. In addition, on the first three days of the campaign, the clouds are cirrus clouds that has delicate to no features. As of September 25, more isolated cumuliform clouds were visible but the camera intervals are positioned too close together that no 3D models were reconstructed from this ground campaign.

Table 3.11 Camera locations for August 22, 2021 Ground Campaign at Shibuya City (13:47 JST – 14:30 JST, Camera Direction at 310° N to 358° N)

	Camera 1	Camera 2	Camera 3	Camera 4	Camera 5
Latitude	35°40’9”N	35°40’10”N	35°40’12”N	35°40’12”N	35°40’8”N
Longitude	139°41’56”E	139°41’47”E	139°41’45”E	139°41’45”E	139°41’47”E

Table 3.12 Camera locations for August 23, 2021 Ground Campaign at Shibuya City (10:47 JST – 14:28 JST, Camera Direction at 31° NE to 71° NE)

	Camera 1	Camera 2	Camera 3	Camera 4	Camera 5
Latitude	35°40’10”N	35°40’9”N	35°40’9”N	35°40’10”N	35°40’13”N
Longitude	139°41’59”E	139°41’56”E	139°41’50”E	139°41’46”E	139°41’44”E

Table 3.13 Camera locations for August 24, 2021 Ground Campaign at Shibuya City (11:47 JST - 15:07 JST, Camera Direction at 29° NE to 111° E)

	Camera 1	Camera 2	Camera 3	Camera 4	Camera 5
Latitude	35°40’10”N	35°40’9”N	35°40’9”N	35°40’10”N	35°40’11”N

Longitude	139°41’59”E	139°41’54”E	139°41’50”E	139°41’46”E	139°41’46”E

Table 3.14 Camera locations for August 25, 2021 Ground Campaign at Shibuya City (10:55 JST – 15:02 JST, Camera Direction at 35° NE to 93° N)

	Camera 1	Camera 2	Camera 3	Camera 4	Camera 5
Latitude	35°40’10”N	35°40’9”N	35°40’9”N	35°40’10”N	35°40’13”N
Longitude	139°41’59”E	139°41’54”E	139°41’50”E	139°41’46”E	139°41’45”E

Table 3.15 Camera locations for August 26, 2021 Ground Campaign at Shibuya City (10:57 JST – 15:05 JST, Camera Direction at 50° NE to 333° NW)

	Camera 1	Camera 2	Camera 3	Camera 4	Camera 5
Latitude	35°40’9”N	35°40’9”N	35°40’9”N	35°40’8”N	35°40’9”N
Longitude	139°41’52”E	139°41’51”E	139°41’50”E	139°41’48”E	139°41’47”E

Table 3.16 Camera locations for August 27, 2021 Ground Campaign at Shibuya City (07:22 JST – 08:39 JST, Camera Direction at 14° N to 345° N)

	Camera 1	Camera 2	Camera 3	Camera 4	Camera 5
Latitude	35°40’9”N,	35°40’9”N,	35°40’9”N,	35°40’9”N,	35°40’7”N,
	139°41’52”E	139°41’51”E	139°41’50”E	139°41’47”E	139°41’47”E
Longitude					

Table 3.17 Camera locations for August 27, 2021 Ground Campaign at Shibuya City (10:02 JST – 15:03 JST, Camera Direction at 217° W to 275° W)

	Camera 1	Camera 2	Camera 3	Camera 4	Camera 5
Latitude	35°40’9”N,	35°40’10”N,	35°40’10”N,	35°40’10”N,	35°40’10”N,
	139°41’52”E	139°41’51”E	139°41’52”E	139°41’50”E	139°41’49”E
Longitude					

On September 26, Diwata-2 captured 24 images of the Kanto region as it traverses from 38.9898º N and 134.1202º E to 31.6064º N and 132.0714º E at time 05:43:26 UTC to 05:45:20 UTC. Landmarks were more visible in the image at time 05:45:20 UTC so it was geo-referenced using the Himawari-8 Band 3 (0.64 μm) image. After geo-referencing, it was observed that the ground camera FoV was within the Diwata-2 FoV. The targeted clouds were predicted to be within the white circle seen in the Himawari-8 image in Figure 3.9. The position of the ground cameras is represented by the red points. Due to the extreme camera rotation of Diwata-2, the target cloud was blocked by another cloud within its FoV.

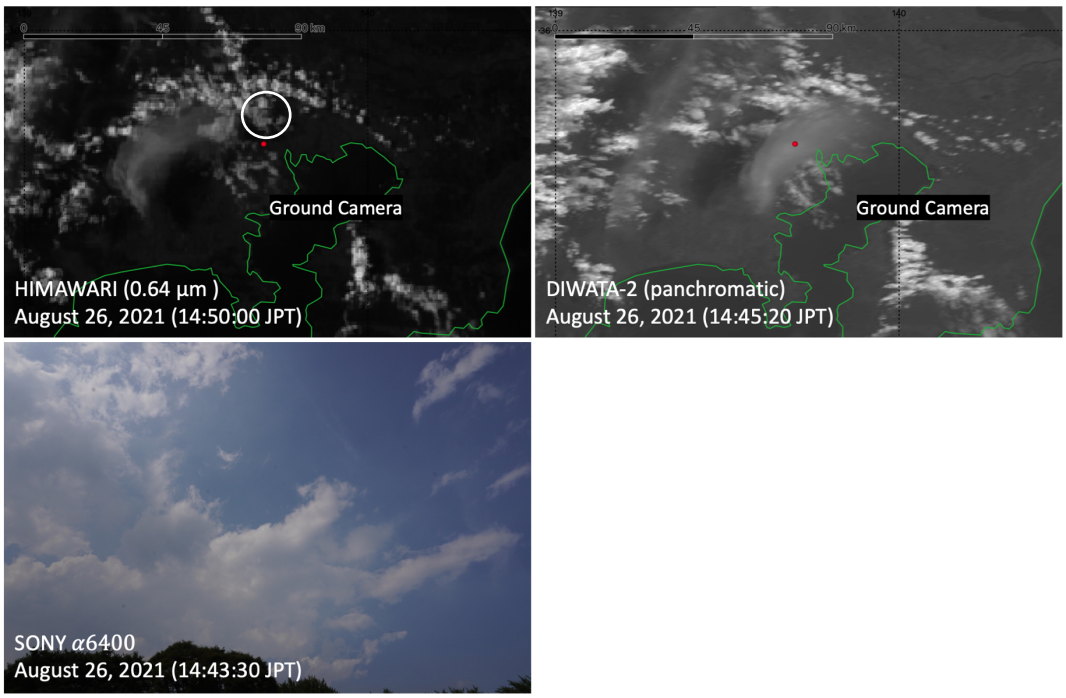

Figure 3.9 Himawari-8 Band 3 image of the Kanto region (top left), geo-referenced image of Diwata-2 (top right), and captured image of Camera 3 during the ground campaign (bottom).

Chapter 4

3D Analysis

The first section of this chapter discusses how stereo-photogrammetry is conducted in this research. This is followed by the methodology of estimating cloud-top altitude from thermal infrared of meteorological satellites.

4.1 Stereo-photogrammetry

The goal of stereo-photogrammetry is to measure the depth or the distance between various points of the cloud in the scene relative to the position of the camera by extrapolating information from stereo images or two slightly offset images (Haralick, 1980; Posner, 2019). Stereo images can be captured by stereo camera (two or more cameras) or monocular camera (single camera). In my research, I used monocular camera for the satellite observation and the aircraft reconnaissance, where I captured stereo images taken by a single camera at different positions. On the other hand, I used 5 stereo cameras for my ground observations.

Triangulation is a method for determining depth from stereo images. Consider the simplest model of binocular stereo geometry. Figure 4.1 shows two identical cameras separated in the x-direction by a baseline distance b. Thus, their optical axis and focal lengths (distance of the camera from x-axis) are parallel and the image planes projected by these cameras are coplanar. The plane passing through the camera centers and the feature point in the scene is called the epipolar. The intersection of the epipolar plane with the image plane defines the epipolar line. Since stereo images are taken at different positions, there is an offset of a feature point from one image to its stereo pair which is called disparity. Disparity is the difference in image location of the same 3D point when projected under the perspective of two different cameras. The disparity is projected along the epipolar line.

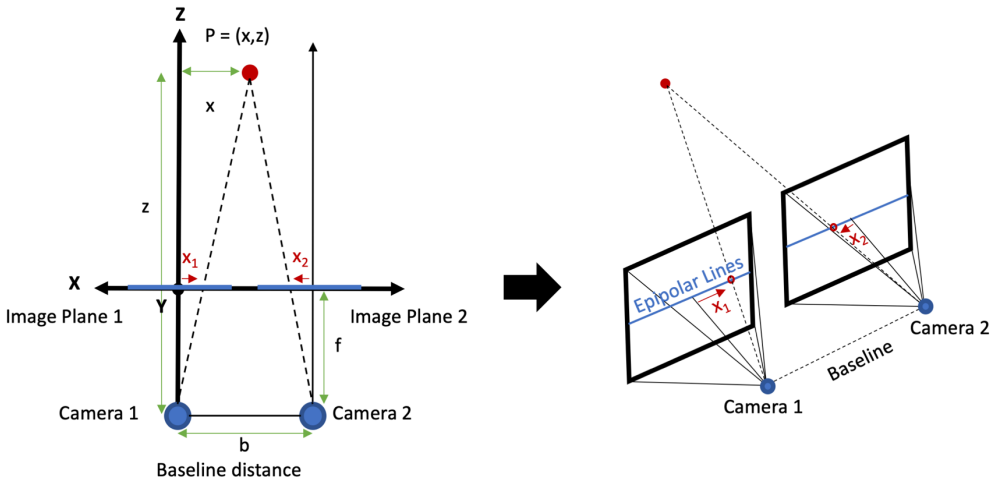

Figure 4.1 Simple stereo-camera setup where the cameras have translation along a single axis (x-axis).

To calculate the depth information of the feature correspondences, we use the concept of Similar Triangles where the corresponding sides will give the following equations

$$\frac{z}{f} = \frac{x}{x_1},$$
$$\frac{z}{f} = \frac{b-x}{-x_2},$$
$$\frac{z}{f} = \frac{y}{y_1} = \frac{y}{y_2}.$$

Equations 4.1

Simplifying the equations, we derive depth z as

$$z = \frac{bf}{d},$$

Equation 4.2

where d is disparity. From here, we can see that the depth is inversely proportional to disparity. It means that if we are moving our camera across the x-axis and we observe a feature point in the scene, the slower the movement of that point across the stereo images, the farther it is from the camera.

If the optical axis of the two stereo-cameras is not parallel just like in Figure 4.2, the epipolar constraint still holds but the epipolar lines will not be horizontal. In this case, the calculation of camera perspective transformation (calculation of position of the physical world features as projected on the 2D image plane) will be more complicated.

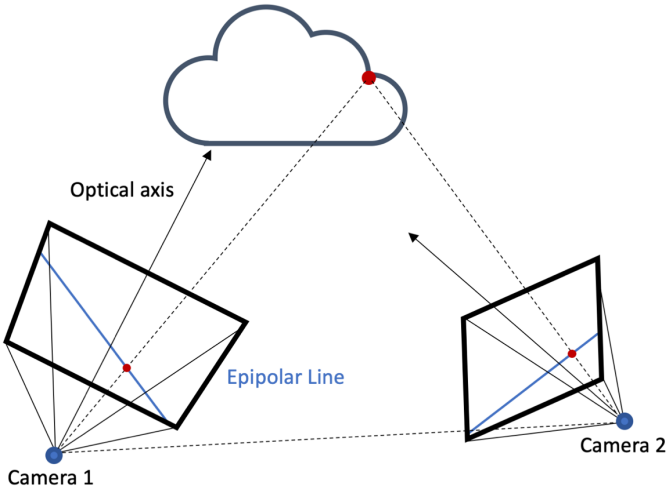

Figure 4.2 Camera setup for cloud stereo-photogrammetry.

However, for the objective of estimating the cloud-top altitude from the ground, ensuring that there is enough image overlap is the most important parameter in setting up the camera position. According to Agisoft Metashape, the recommended amount of image overlap for aerial photography should at least be 60% side overlap and 80% forward overlap. However, for forest surveys, it is recommended to increase the overlap value to 80% and 90% respectively (Agisoft LLC, 2021). We can assume that the cloud survey is similar to a forest survey due to the absence of rigid features. According to multiple observations, the closest possible distance of a target cloud to the camera where the cloud features are still within the image frame is around 1.5 km. Using this information, an interval of 200m between cameras should be enough to ensure that there is at least 92% image overlap between images. Since the field location is usually conducted in an open area of high-density cumulonimbus clouds, the location of the camera is not predetermined. From trial and error, the amount of overlap is enough to compensate for the unknown camera rotation and forward overlap that will be used to point at a target cloud in the field.

The usual approach in estimating cloud-top altitude from satellite images is stereoscopy. Stereoscopy uses parallax information to perceive depth from images of the subject at different viewing angles. In meteorology, most stereoscopic techniques use multiple geostationary satellites that capture target clouds. However, the accuracy of these techniques is dependent on the acquisition-time difference between two satellites since their capture time are not usually synchronized. Conversely, there are stereoscopic systems that utilize a single satellite that either has multiple cameras capturing images at the same time or a single camera capturing images at different locations. These setups have the advantage of near-simultaneous capture, but there are only few satellites that guarantee high temporal resolution data.

These techniques in stereoscopy prove to be challenging as cloud features required for stereo-matching might not be visible and rigid due to cloud advection and morphology deformation. Most satellites take minutes between capture, creating large angle and distance between captured images. This makes it difficult for the stereoscopy algorithms to detect matching features between images. Thus, if the angles between two images are too large, the overlapping features between the images might be insufficient.

In this research, images are taken at a high temporal resolution (30s or less) and at optimized viewing angles. Cloud features were also enhanced using GIMP software to help the algorithm find stereo pairs among the images. The images were loaded in a 3D imaging software, Agisoft Metashape 1.5.2.7837, that outputs both a Digital Elevation map (DEM) and an orthomosaic (2D projection of the 3D model) (Agisoft Helpdesk Portal, 2020). The software uses semi-global matching and mutual information to detect stereo correspondences between images (Hirschmuller, 2008). Photogrammetric point cloud is generated using information from these stereo correspondences and a 3D model is reconstructed by creating a mesh from these point clouds. Since these points are sparse, texture is added to the model by overlaying the image on the mesh to create photorealistic digital representation of the typhoon. The software solves the camera's relative orientation, generates depth maps, and reconstructs the surface of the cloud. However, since we are using the 3D model to measure world features (cloud-top altitude), the initial camera rotation should be known to be able to correct the global rotation of the stereo-photogrammetric model.

Image Overlap

To measure the actual overlap between adjacent images, image correlation was performed. Prior to correlation, the images were converted to Grayscale to eliminate the influence of different image white balancing effect contributed by the cameras on the correlation result.

Correlation was used to measure the similarity in the patterns of the images that is expressed mathematically by

$$p(x,y) = \iint f(x',y')g(x+x',y+y')\,dx'dy'$$

where f(x, y) and g(x, y) are two-dimensional functions. Equation 3.6 measures the association between the two functions and is simplifed by the notation '⊙'. Correlation is related to convolution by

$$p = f \odot g = f(-x,-y) * g(x,y)$$

where the function f is in complex conjugate. Using the Convolution Theorem given as

$$F\{f * g\} = F\{f\} \cdot F\{g\}$$

the correlation could be expressed into

$$p = F^{-1}\{F\{f(-x,-y)\} \cdot F\{g(x,y)\}\}$$

where are F is the Fourier Transform of the function given as

$$F(k) = \int_{-\infty}^{\infty} f(x)e^{-2\pi ikx}dx$$

The higher the similarity, the more correlated the images are. On the correlated image, the white peaks implies that it has the maximum correlation.

4.2 Cloud-top Altitude Estimation from Brightness Temperature

We compared the altitude profiles of the cloud-top altitude estimated from the stereo-photogrammetry and the estimated value from HIMAWARI-8 satellite's TIR.

A standard method of estimating the cloud-top altitude from a satellite's TIR is by converting it to brightness temperature (BT) (Bosisio & Mallet, 1998). In this research, we acquire the relationship of temperature with cloud-top altitude through linear regression using measurements taken by dropsonde. However, dropsonde measurements are difficult to deploy and data are limited. In our case, we did not deploy dropsondes during the Typhoon Maysak and cumulonimbus cloud observations. We also did not utilize the T-PARCII dropsonde data since the data set is too small to see any correlation between the temperature and the cloud-top altitude. To make up for this we used data from National Oceanic and Atmospheric Administration (NOAA) as replacement. NOAA has an archive of dropsonde data for each hurricane within the Atlantic and the East Pacific (National Oceanic & Atmospheric Administration, 2018). Since the height of atmospheric layers and clouds vary with latitude, the dropsonde data from NOAA that should be used for cloud-top estimation should be taken at the closest distance with similar latitude range to the typhoon being analyzed. Furthermore, the closer the time of the dropsonde deployment to the occurrence of the typhoon, the more ideal it would be. For an instance, Typhoon Trami ranges from 17°N to 26°N (Mack, Hasler, & Rodgers, 1983). On the other hand, Hurricane Hector is a category 4 hurricane that hit the East Pacific Basin last August 2018 with latitude range of 12°N to 22°N. Because of the large latitude overlap between the two tropical cyclones, it is reasonable to use the data from Hurricane Hector BT-cloud height relationship with Typhoon Trami data.

Clouds form at a relative humidity (RH) of 95-100% (Bosisio & Mallet, 1998). To estimate the cloud-top altitude from dropsonde data, we take the highest altitude where the RH is at least 95%. The cloud-top altitude is plotted with temperature (Figure 4.3) and their linear regression is obtained. Finally, the cloud-top altitude was estimated using the BT and the previously calculated cloud-top and temperature relationship from dropsonde data. This is working on the assumption that the relationship of the cloud-top altitude and temperature is linear which is not the same for all kinds of clouds.

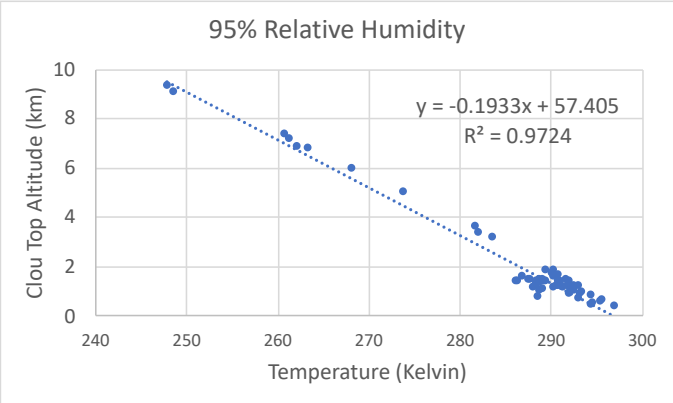

Figure 4.3 Plot of cloud-top altitude (with RH of 95%) vs. Temerature

Chapter 5

Results

This section shows the output of the experiments conducted during the span of the research. The information extracted from the stereo-photogrammetric model, as well as the accuracy of the models, were discussed.

5.1 Satellite Observation for Typhoon Maysak

The satellite images of Typhoon Maysak from the third observation of Diwata-2 taken last September 2, 2020 (05:51:10 UTC to 05:51:15 UTC) were used for the stereo-photogrammetry. The images from Diwata-2 were georeferenced by comparing cloud features with images from Himawari-8 Band 3 (06:00:00 UTC) of known geo-locations. Six geo-references were selected based on the clarity of the matching cloud features visible from both satellite images. These were used to improve the accuracy of the position and scale of the model. The blue points indicate the position of the geo-references used in the model as seen from Figure 5.1.

Agisoft Metashape was able to detect a total of 3,228 matched points between two or more images with a 2.64 pix RMS reprojection. The deep parts of the typhoon eye as well as the ridges/protrusions from the spiral rain bands were visible from the 3D model. It took 4 minutes and 56 seconds to process the model from feature matching to surface reconstruction using an iMac with an Intel Core i5-8600 processor at 3.1GHz, an 8GB RAM, and a Radeon Pro 575X graphics card.

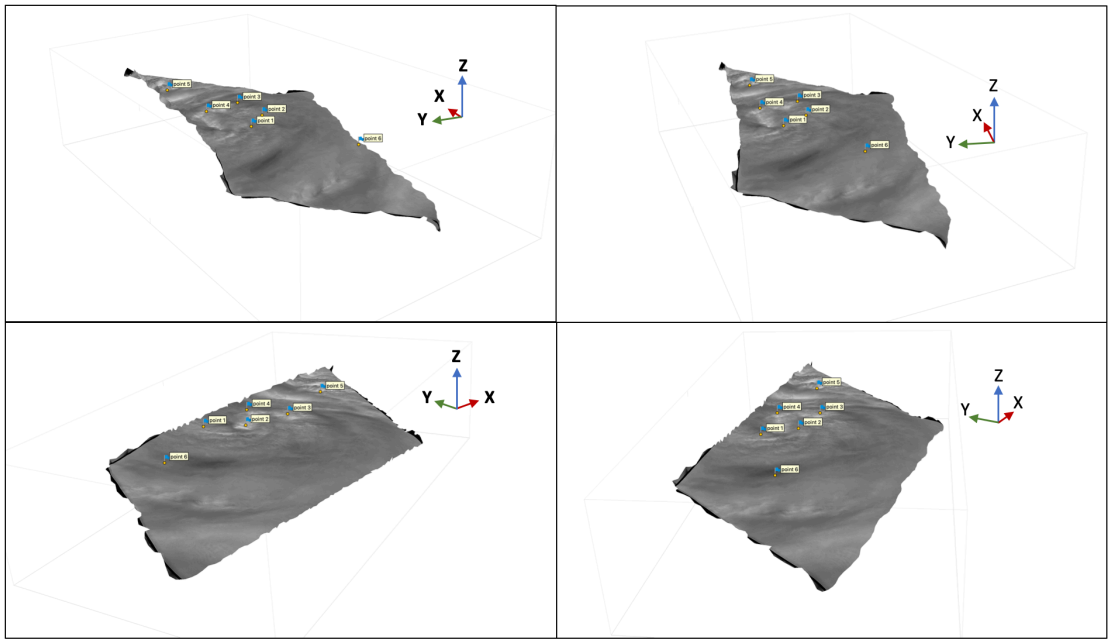

Figure 5.1 The four images show Typhoon Maysak 3D reconstruction at different view angles.

Himawari-8 Band 3 image (0.64μm) taken at 05:50:00 UTC on September 2, 2020, which is the closest capture time with the aircraft images, was used to validate the position of the orthomosaic map as shown in Figure 5.2. The area coverage of the model is approximately 33,100 km^2 with ground resolution of 103 m which is the area of the ground covered by one pixel of the orthomosaic. The model has a latitude range of 31.1˚N to 32.2˚N and longitude range of 126.1˚E to 129.4˚E.

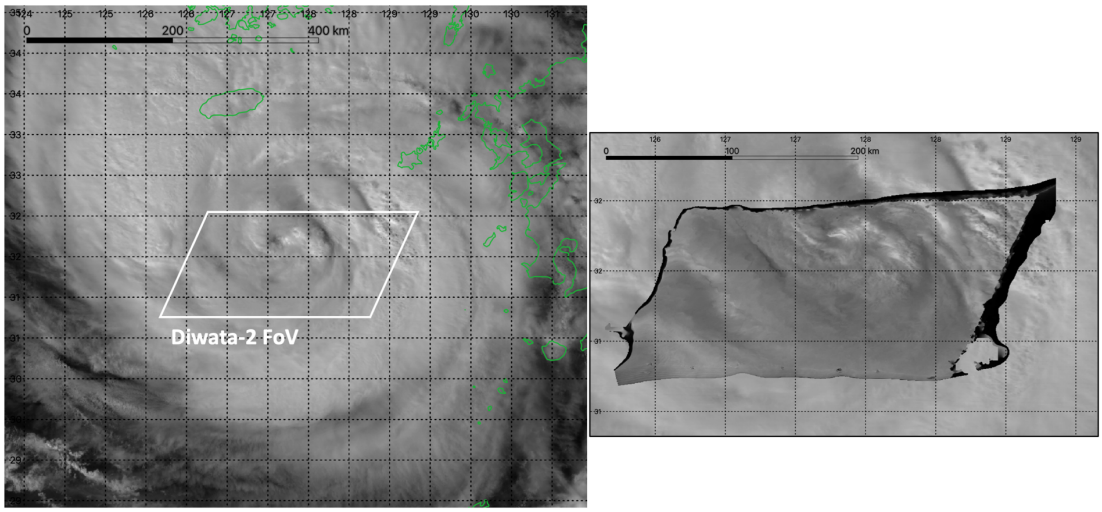

Figure 5.2 Left: Typhoon Maysak as captured by the Himawari-8 satellite. Right: Area coverage of the Typhoon Maysak orthomosaic as seen on top of the satellite image.

5.2 Aircraft Campaign for Typhoon Trami

From the aircraft reconnaissance taken on September 26, 2018 (05:56:44 UTC to 05:56:59 UTC), 8 stereoscopic images were selected based on the image clarity and the amount of image feature overlap. These were used for the stereo-photogrammetry

where a total of 8,715 matched points was detected by Agisoft Metashape with 2.37 pix RMS reprojection error. The area coverage of the model is approximately 2,080 km^2 with ground resolution of 6.08 m. The ground resolution of the model is higher for the aircraft images than the satellite images since the image source is closer to the subject and this also resulted to smaller projection error. It took 8 minutes and 43 seconds to process the model from feature matching to surface reconstruction using the same machine from Typhoon Maysak DEM reconstruction.

From the visual inspection of the images, the clouds on the horizon should be leveled. However, this did not correspond to the depth map of the model since the camera rotations were not known and were not considered in the surface reconstruction. Applying the assumption that the horizon should be level, we calculated the camera roll, camera rotation along its y-axis, based on the highest and lowest point of the depth map which are 11.3 km and -8.87 km respectively. The two altitudes are approximately 55.1 km apart, resulting to an estimated camera roll angle of 20.1°. The estimated camera roll angle was then used to correct the DEM orientation as shown in Figure 5.5.3.

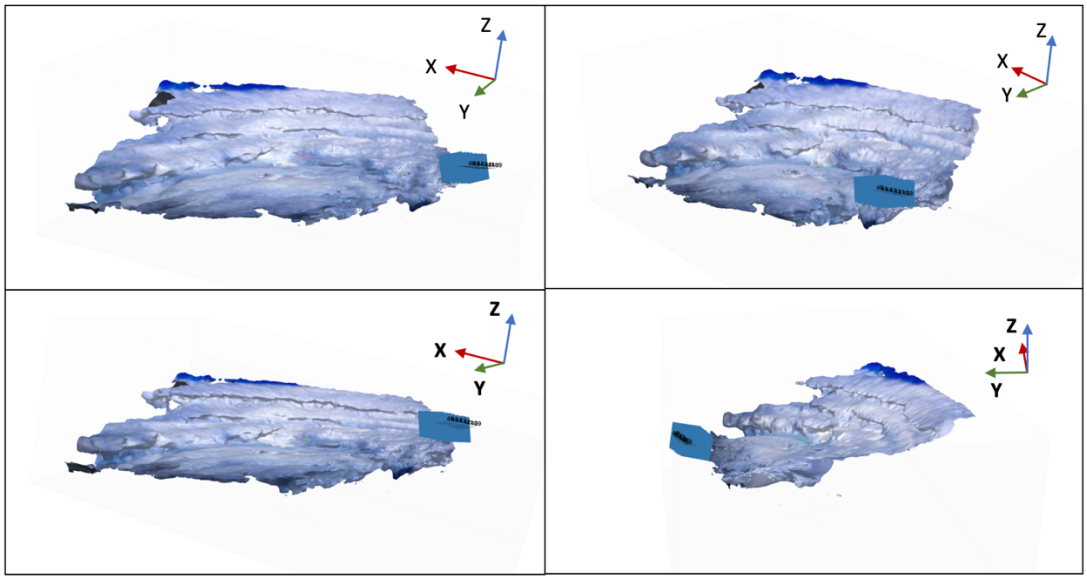

Figure 5.5.3 The four images show Typhoon Trami 3D reconstruction at different view angles. Typhoon Trami images were overlaid on the 3D mesh based on their alignment, generating color gradients and lighting information on the model's surface.

Himawari-8 Band 3 image (0.64μm) taken at 06:00:00 UTC on September 26, 2018, which is the closest capture time with the aircraft images, was used to validate the position of the orthomosaic map as shown in Figure 5.4. The orthomosaic has latitude range of 20.4°N to 20.9°N and longitude range of 128.8°E to 129.6°E.

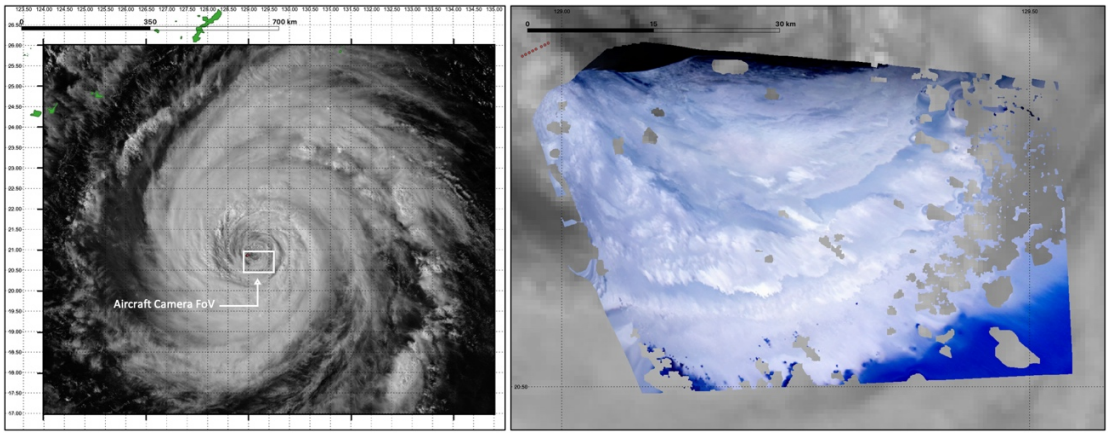

Figure 5.4 Left: Typhoon Trami as captured by the Himawari-8 satellite. Right: Area coverage of the Typhoon Trami orthomosaic as seen on top of the satellite image.

The DEM of Typhoon Trami was used to estimate the cloud-top altitude of a portion of the its eye and eyewall. The estimated maximum and the minimum altitude from the DEM is $14.3km \pm 2km$ and $1.3km \pm 2km$ respectively.

5.3 Ground Campaign

5.3.1 2019 August 14 Tokyo Fieldwork

For the ground observation conducted on August 14, 2019 (14:25 JST), only three out of the five images were successfully matched by Agisoft Metashape. This means that the image overlap between the other two cameras were too small. The software detected a total of 497 stereo correspondences with 3.2 pix RMS projection error. The reconstructed 3D model is shown in Figure 5.5. The model was colored by overlaying an image on the mesh. The estimated cloud-top altitude from stereo-photogrammetry is 6.2 km and an area coverage of 151 km^2 with a ground resolution of 4.5m. The reconstructed cloud has latitude range of approximately 35.9467°N to 35.7382°N and longitude range of 139.9026°E to 139.9467°E. From the orthomosaic, however, the orientation of the model does not correspond with the position of the cloud in Himawari-8 image with latitude ranging from 35.5144°N to 35.65301°N and longitude range of 139.8492°E to 139.9001°E. In addition, the scale of the model is also larger than the size of the full cloud.

5.3.2 2020 September 5 Tokyo Fieldwork

For the ground observation conducted on September 5, 2020 (16:18 JST), all five images were successfully matched by Agisoft Metashape. This resulted to more detected matched points of 617 stereo correspondences with 4.34 pix RMS projection error. The reconstructed 3D model is shown in Figure 5.6. Image texture was also overlayed on the model to create color gradient and shading effect. Relative to the previous output, the model has higher resolution and more visible cloud texture. The estimated cloud-top altitude from stereo-photogrammetry is 3.4 km and an area coverage of 4.27 km^2 with a ground resolution of 1.85 m. The reconstructed cloud has latitude range of approximately 35.6°N to 35.7°N and longitude range of 139.85°E to 139.95°E.

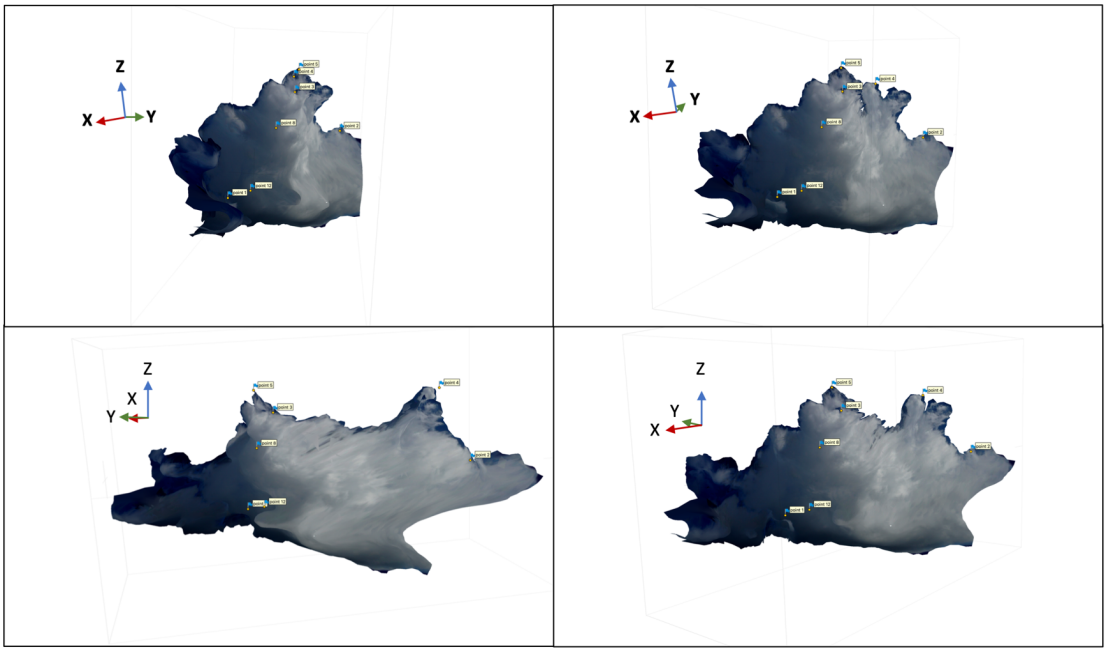

Figure 5.5 Four views of the stereo-photogrammetric model of an isolated cumulonimbus cloud from August 14, 2019 ground observation. The four view angles were selected based on the optimal view of the model's features.

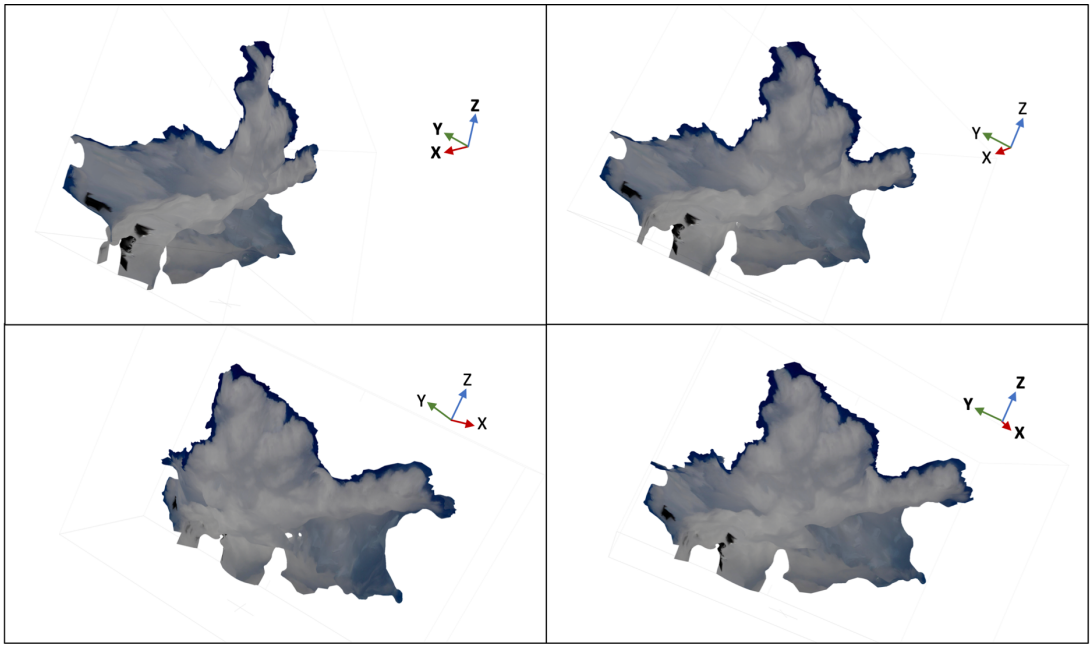

Figure 5.6 Four views of the stereo-photogrammetric model of an isolated cumulonimbus cloud from September 5, 2020 ground observation. The four view angles were selected based on the optimal view of the model's features.

Chapter 6

Discussion

This chapter shows the comparison of the cloud-top altitude estimated from both stereo-photogrammetric method and the thermal infrared. It also covers the scientific interpretation of the research output.

6.1 Comparison of Stereoscopic-based cloud-top profiles with TIR Brightness Temperature

This research aims to improve the accuracy of typhoon intensity estimation using stereo-photogrammetry from different imaging sources: satellite images, aircraft images, and ground camera images. Different imaging sources cater to different temporal and spatial scale requirements of the cloud observations in this research. We reconstructed high resolution 3D models of typhoons, typhoon eyes, and isolated cumulonimbus clouds as shown in the previous chapter. From these models, we were able to see cloud structures that correspond to some atmospheric phenomena that has not been fully observed visually before such as eyewall replacement cycle that will be shown in this chapter.

We compared the cloud-top altitude profile estimated from the stereo-photogrammetry to the estimated values from HIMAWARI-8 satellite's thermal infrared band (TIR). To perform this, the DEM was loaded to Blender, a 3D visualization software where it can also be overlaid on Google Maps. Each point on the DEM corresponds to an altitude value. Segments across the DEM were extracted as altitude profiles. Upon comparison with the orthomosaic map, the corresponding altitude profiles from the TIR were determined.

To get the cloud-top altitude estimate from TIR for Typhoon Maysak observation, we used the NOAA dropsonde data of Hurricane Nana. Hurricane Nana is a tropical cyclone that hit Belize and Mexico in early September 2020. It developed on September 1, 2020 traversed from latitude of approximately 16°N to 28°N as it dissipated on September 4, 2020. The relationship of the cloud-top altitude with temperature was acquired through linear regression is

$$y = -0.1738 * BT + 52.129 \qquad \textbf{Equation 6.1}$$

where y is the cloud-top altitude in kilometers. It has an R^2 of 0.89 and standard deviation of 0.56km. Using $\boldsymbol{y = -0.1738 * BT + 52.129}$ **Equation 6.1**, the cloud-top altitude of Typhoon Maysak was estimated. Its maximum cloud-top altitude is 17.2 km and the mean altitude is 13.1 km. Figure 6.1 shows the side-by-side comparison of Typhoon Maysak's DEM and orthomosaic overlayed on cloud-top

estimate from TIR. The orange lines represent the five altitude profiles on the DEM and their corresponding position on the cloud-top from TIR.

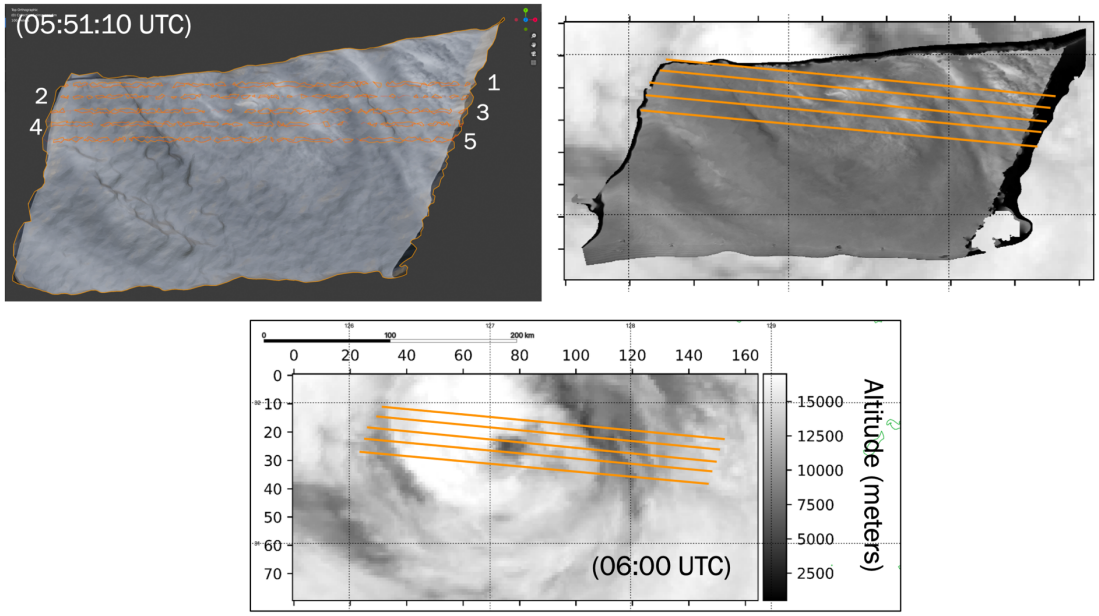

Figure 6.1 The five selected typhoon cloud altitude profiles that will be analyzed as represented by the orange lines on the DEM (top left) and orthomosaic (top right) of Typhoon Maysak. (Bottom) The corresponding orange lines as projected on the estimated cloud-top altitude from TIR.

The altitude profiles estimated from the stereo-photogrammetry and TIR were plotted in Figure 6.3 for visual comparison. The estimated maximum cloud-top altitude from the stereo-photogrammetry is 16 km. However, from the altitude profiles, some region of the DEM is too small and this is attributed to the error that comes from the unknown camera rotation, creating a DEM that is also rotated to one side as shown in Figure 6.2. However, it is important to note the similarity in the cloud structure between the two methods. Stereo-photogrammetry were able to detect detailed cloud structure of Typhoon Maysak.

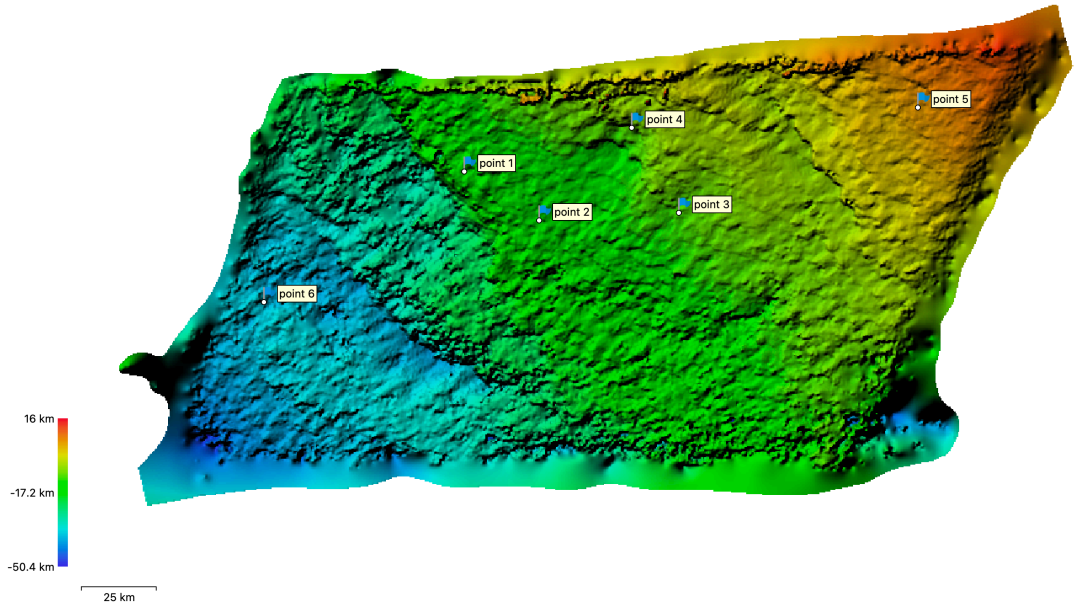

Figure 6.2 DEM of Typhoon Maysak

To estimate the cloud-top altitude of Typhoon Trami from Himawari-8 TIR, dropsonde data of Hurricane Hector that was extracted from NOAA archive was utilized as mentioned in section 4.2 of this thesis. The relationship of the cloud-top altitude with temperature was acquired through linear regression with R^2 of 0.97 and standard deviation of 2.13km.

$$y = -0.1933 * BT + 57.405. \qquad \text{Equation 6.2}$$

With this known altitude-temperature relationship, the cloud-top was estimated by converting the TIR of the region covered by the Typhoon Trami orthomosaic. The maximum cloud-top altitude is 21.1 km and the mean altitude is 4.2 km. Three cross-sections were extracted from the DEM as represented by the three red lines in Figure 6.4. Segment 1 cloud-top altitude ranges from 3.83km to 12.9km, segment 2 ranges from 5.75km to 14.4km, and segment 3 ranges from 5.93 to 13.2km. The maximum cloud-top estimate from stereo-photogrammetry is within reasonable height as clouds at typhoon eyewall can be as low as 400 meters and rise up to 15 km (Zehnder, 2021). The error from stereo-photogrammetry can be attributed to the RMS projection error and camera resolution of the 3D reconstruction. For the cloud-top altitude from TIR approach, the sources of error are attributed to the assumption that the cloud-top-temperature relationship is linear, the difference in dropsonde and satellite temperature measurements and the warm thermal bias of typhoon center. The thermal bias is involved when using TIR-approach as the eyewall is warmer relative to other regions of the typhoon.

For the ground camera observations, the stereo-photogrammetric model is reconstructed such that the surface is facing the direction of the cameras from the ground. On the August 14, 2019 (14:25 JST) observation, the camera bearing ranges from 177° N to 219° N thus, the cloud surface is facing northward. Five vertical profiles were selected across the width of the cloud model, approximately 500m to 700m apart, as shown in Figure 6.6. These lines with width ranging from 100m to 150 meters wide

were selected based on the most textured region across the surface. The altitude and the surface profile were plotted in MATLAB as seen in Figure 6.7. From the stereo-photogrammetric model the estimated cloud-top altitude is 6.2 km which is higher by 2.5 km than the maximum cloud-top estimated from TIR of 3.7 km.

On the September 5, 2020 (16:18 JST) observation, the cloud surface is facing eastward. Five vertical profiles were selected across the width of the cloud model as shown in Figure 6.8. The surface profiles were plotted in MATLAB as seen in Figure 6.9. From the stereo-photogrammetric model, the estimated cloud-top altitude is 3.4 km which is higher by 1.7 km than the maximum cloud-top estimated from TIR of 1.7 km.

For both the cloud-top altitude estimates conducted during the ground observation, the estimate from the stereo-photogrammetric method is higher than the TIR method. This huge altitude difference could also be due to BT contamination from surface emissivity as the observations were conducted near or on land. The resolution of the TIR is small (2 km ground resolution) that the emissivity from the surface and from the clouds are difficult to differentiate.

Results show how valuable the resolution is to estimating cloud-top, especially to isolated cumulonimbus clouds that have small scale sizes. Currently, we rely on satellite images to analyze typhoons, but this will only give us information regarding its morphology and location. However, cloud altitude and cloud profiles are also important parameters in estimating intensity and precipitation rate of typhoons and cumulonimbus clouds. If we want to estimate cloud altitude, radar or BT from TIR are commonly used. Radar can output altitude profiles, but this data is very limited, and it cannot detect small-scale clouds. Thermal infrared, on the other hand, can be unreliable due to surface emissivity as seen on our ground observations, and has thermal biases relative to different regions of the typhoon. Stereoscopy can be used to estimate locations of some cloud features (point clouds) using multiple images of the target cloud at different viewing angles, but this does not give enough information on the actual structure of the cloud. In addition, stereoscopy was never conducted using multiple ground cameras alone and requires satellite information. In this study, an actual three-dimensional model was reconstructed from stereo-photogrammetry and typhoons and isolated clouds were analyzed in volumetric perspective. Cloud altitude was estimated from 3D models and cloud profiles were observed.

Though this technique cannot replace the standard method of cloud-top estimation, such as radar data and TIR, it provides a new way of viewing clouds as 3D structures and not as water particles (such as in radars) or temperature (such as in TIR). Stereo-photogrammetry is also not limited to satellite images but could also be done using other imaging sources.

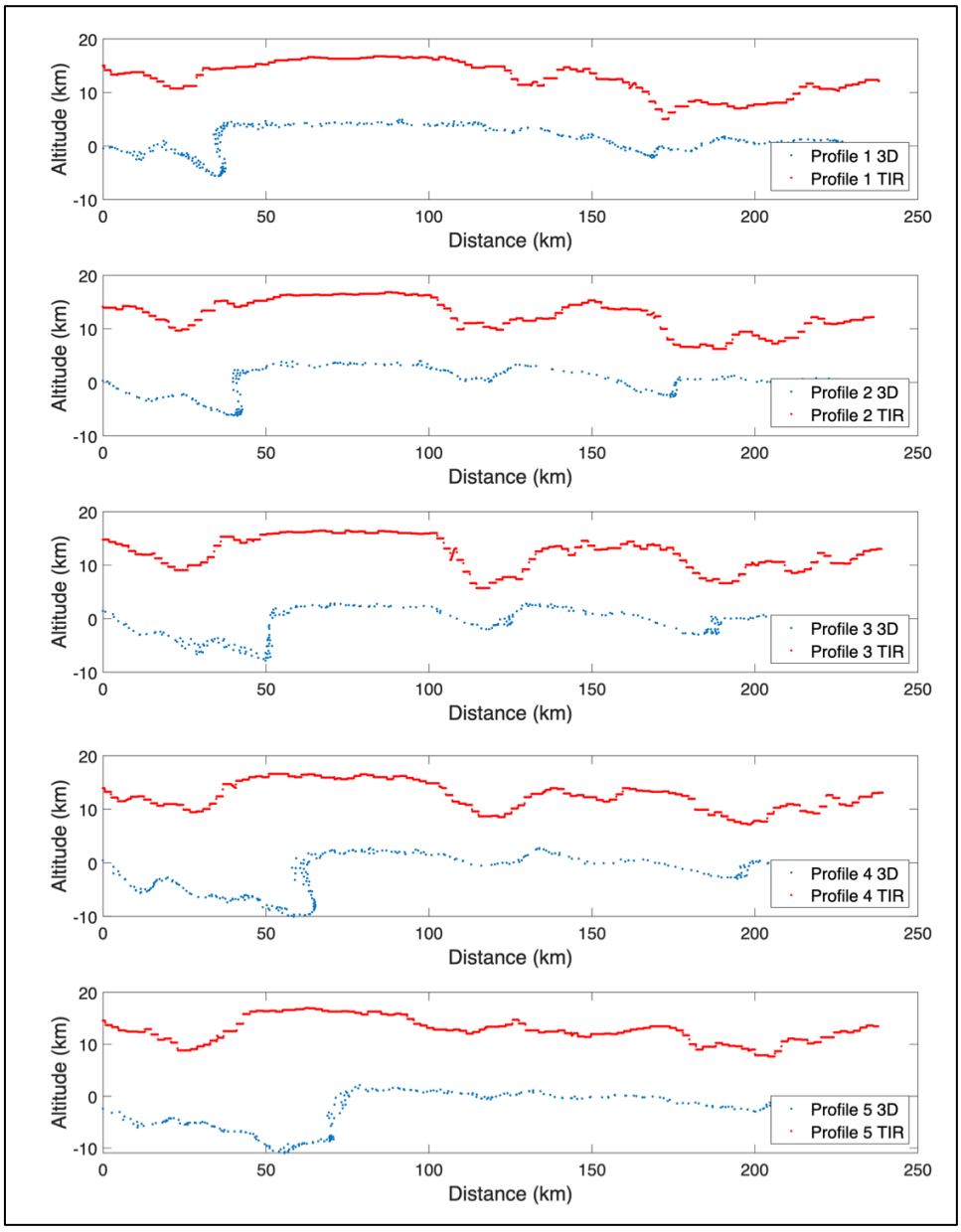

Figure 6.3 The blue points are point clouds of 5 segments derived from the stereo-photogrammetry model of Typhoon Maysak. The red lines represent their corresponding estimated cloud-top altitude calculated from Himawari-8 TIR.

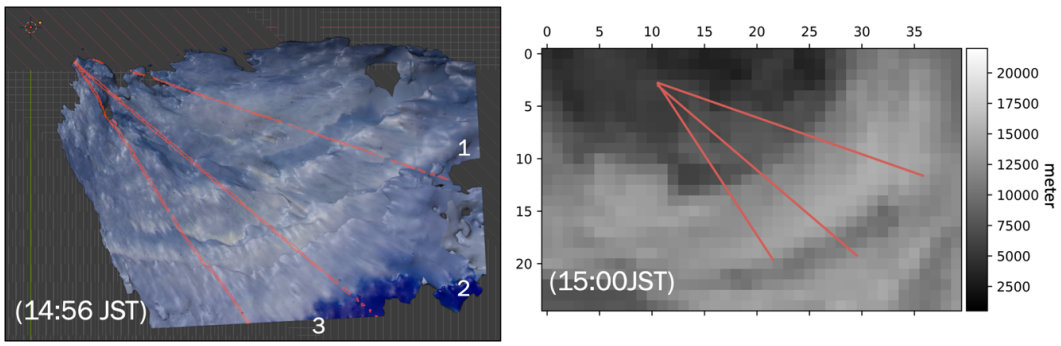

Figure 6.4 (Left) Top view of the Typhoon Trami DEM with the three selected typhoon cloud altitude profiles that will be analyzed as represented by the red lines. (Right) The

cloud-top altitude estimated from Himawari-8 TIR with the three corresponding typhoon cloud altitude profiles that will be analyzed as represented by the red lines.

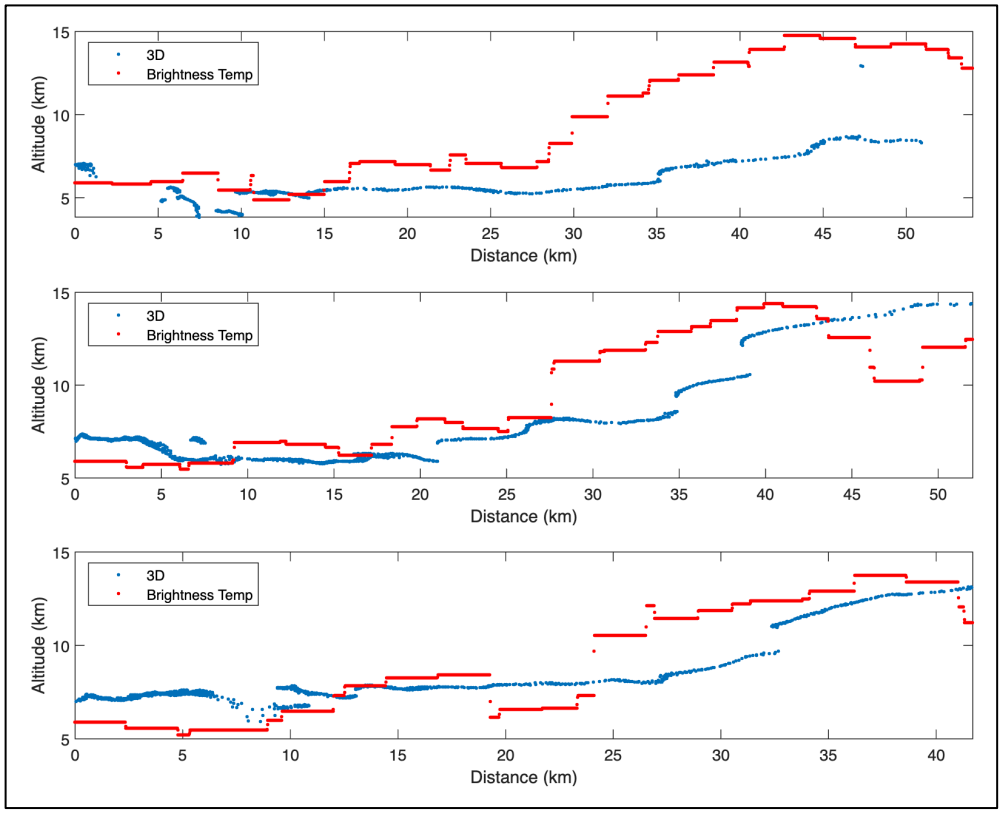

Figure 6.5 The blue dots are point clouds of segments 1, 2 and 3 derived from the stereo-photogrammetry model. The red lines represent the estimated cloud-top altitude calculated from Himawari-8 TIR.

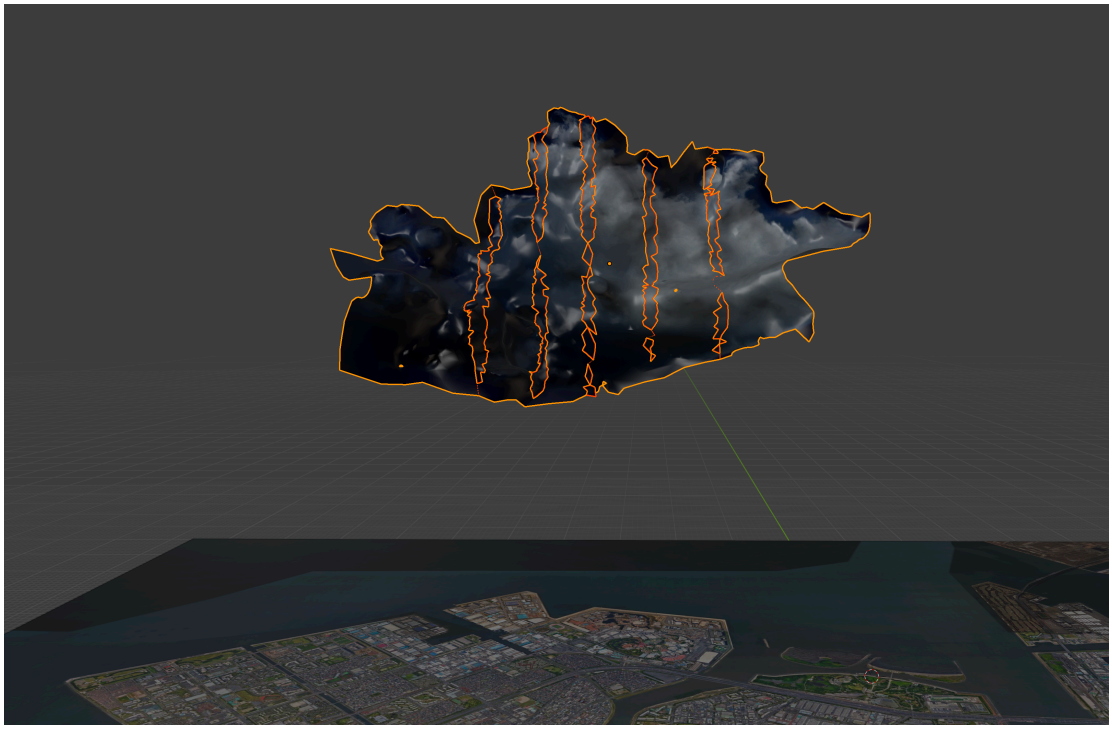

Figure 6.6 Top view of the isolated cloud DEM with the five selected isolated cumulonimbus cloud surface profiles that will be analyzed, represented by vertical regions with orange border lines.

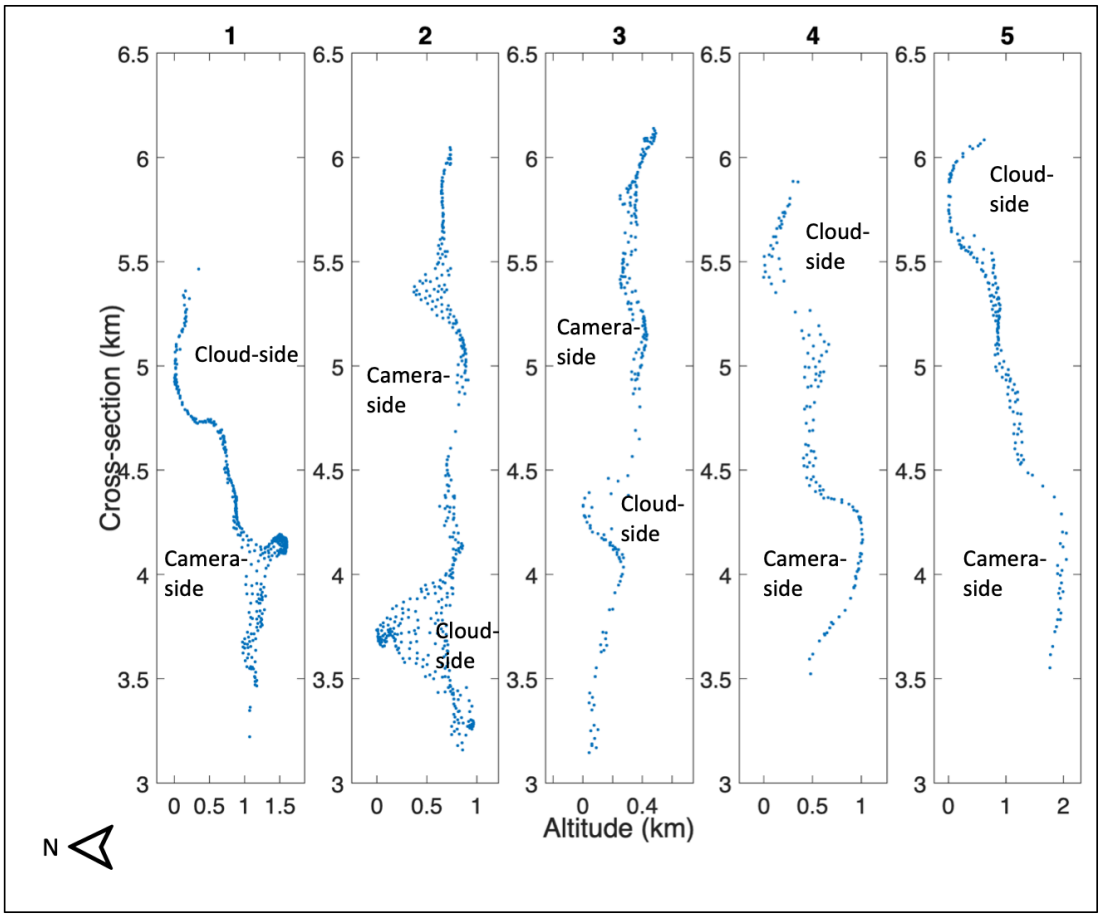

Figure 6.7 Vertical cross-section of an isolated cumulonimbus cloud 3D model from August 14, 2019 ground observation.

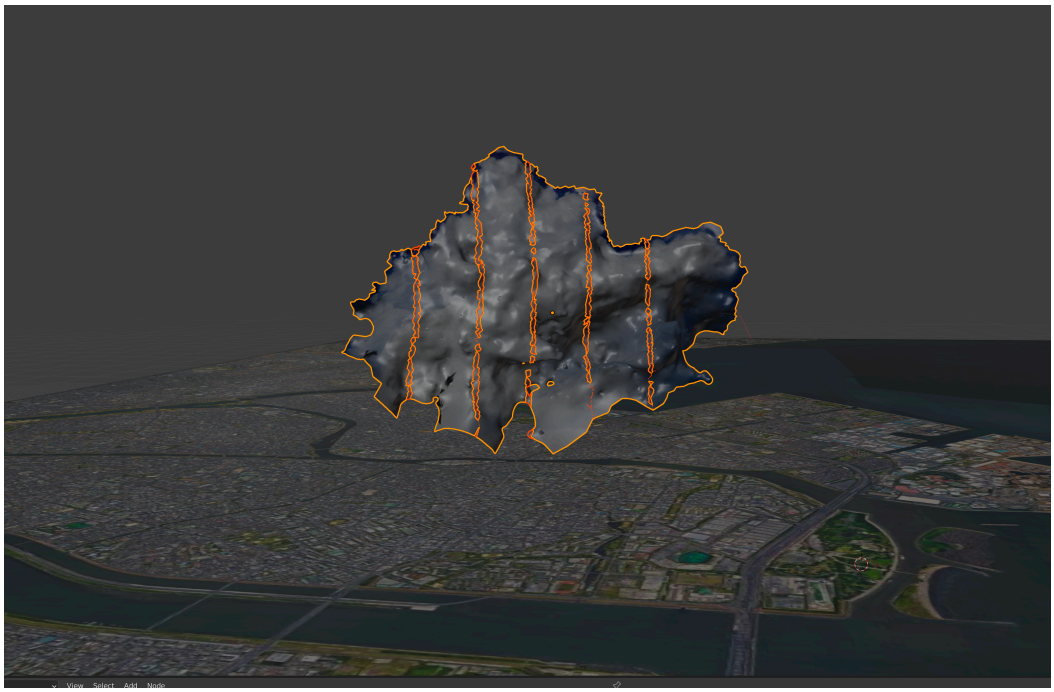

Figure 6.8 Top view of the isolated cloud DEM with the five selected isolated cumulonimbus cloud surface profiles that will be analyzed, represented by vertical regions with orange border lines.

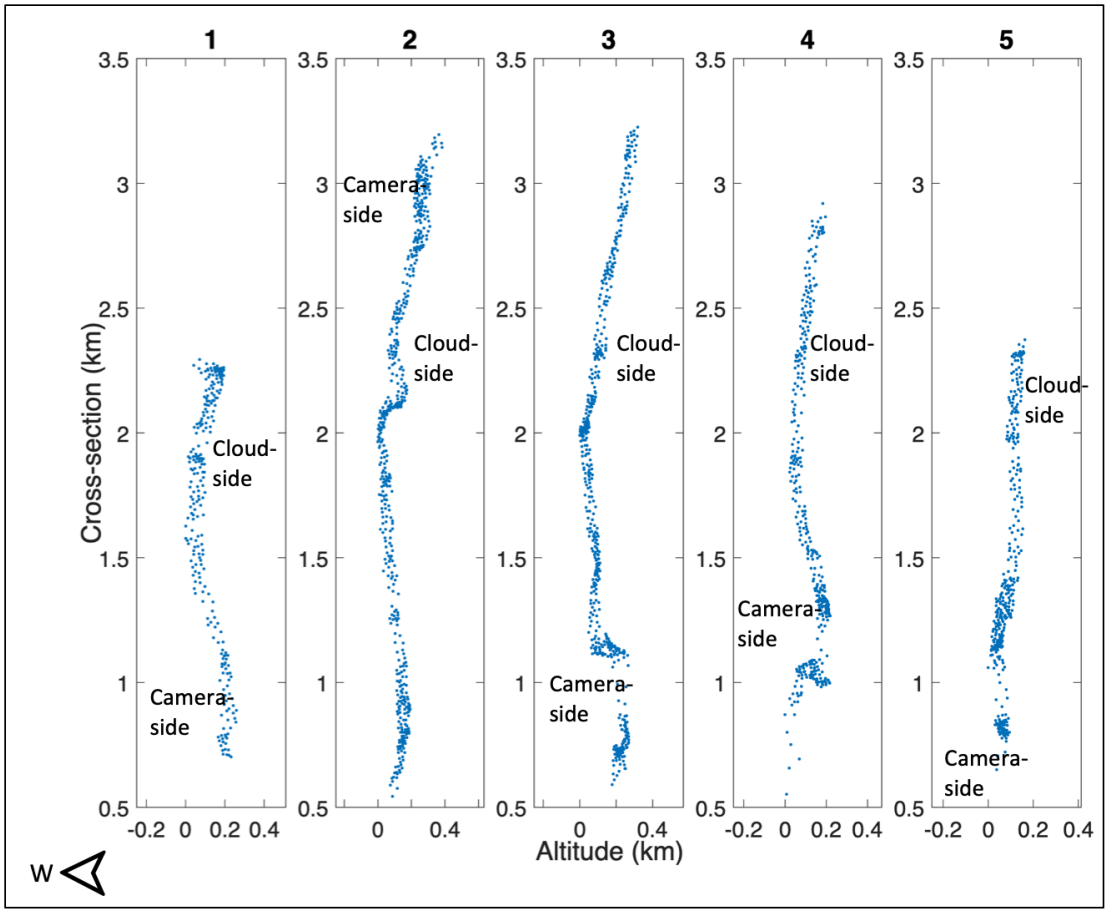

Figure 6.9 Vertical cross-section of an isolated cumulonimbus cloud 3D model from September 5, 2020 ground observation.

6.2 Comparison of Stereoscopic-based cloud-top profiles with Radar

Radar is another way of estimating the cloud elevation by measuring the reflectivity of water droplets present in clouds. During the ground observation conducted on August 14, 2019 (05:25 UTC), ka-band measurement around the Edogawa region was also conducted. Figure 6.10 and Figure 6.11 shows the 6 ka-band measurements captured approximately 1 minute before and 1.5 minute after the ground camera observation. The red circle at capture times 05:24:27 UTC and 05:26:04 UTC indicate the position of the target cloud before and after the ground observation. The observation for elevation angles 2.2°, 6.5°, 15°, 20° are conducted every 2 minutes while for elevation angle 10° is conducted every 4 minutes. The radar is located at latitude 35.76536°N and longitude 139.88758°E with altitude of 24m. Relative to the radar, the target cloud has a distance ranging from 16 km to 27 km across its length, however, basing on how the 3D model is positioned in front of the cloud, we'll assume that the target cloud has a distance of 18 km. From this information, the altitude of the target cloud across its height is 691 m to 2.05 km. The target cloud (Figure 6.10 and Figure 6.11) was not detected at 05:22:49 UTC, 05:25:10 UTC, 05:25:31 UTC, and 05:26:49 UTC because the elevation angle is too large (10°, 15° and 20°) to detect low-lying clouds. Unlike the 3D model that shows a continuous range of cloud-top altitude, it is difficult to measure the actual cloud-top height from ka-band radar because of its low-temporal resolution. Since the target cloud is not visible at 10° elevation angle, we can assume that its cloud-top altitude is lower than 3.20 km.

The estimated cloud-top altitude from stereo-photogrammetry ranges from 3 km to 6.2 km which is higher than the radar measurement and even most low-lying cumuliform clouds which can go up to 5 km (Stull, 2018). However, it is important to note that among the reconstructed models, the August 14, 2019 observation has a larger projection error than the 3D models that use elevated images since only 3 images out of 5 were able to detect stereo correspondences. In addition, the scale, and the position of the model's orthomosaic does not correspond to the target cloud as seen in Himawari-8 image, as previously presented in Subsection 5.3.1.

The estimated cloud height using both techniques did not have an overlap but for scale comparison, the lateral range of the captured cloud is shown. Five lateral segments with thickness of 200m to 300m at different altitudes were extracted from the clouds and plotted in MATLAB as shown Figure 6.12. Each segments have a altitude difference ranging from 300m to 400m apart. The lowest segment at 4 km altitude has a profile length of 4.7 km while the highest profile at 5.4 km altitude has a profile length of 4 km. The maximum cloud width from stereo-photogrammetry is 5.6 km measured at altitude 5.0 km. The estimated lateral cloud size based on the satellite and radar data is at most 5 km. Comparing the estimated maximum lateral profile, there is a 0.6 km discrepancy between the lateral scale of the said techniques, showing that the scale of the 3D cloud model is larger than its satellite counterpart.

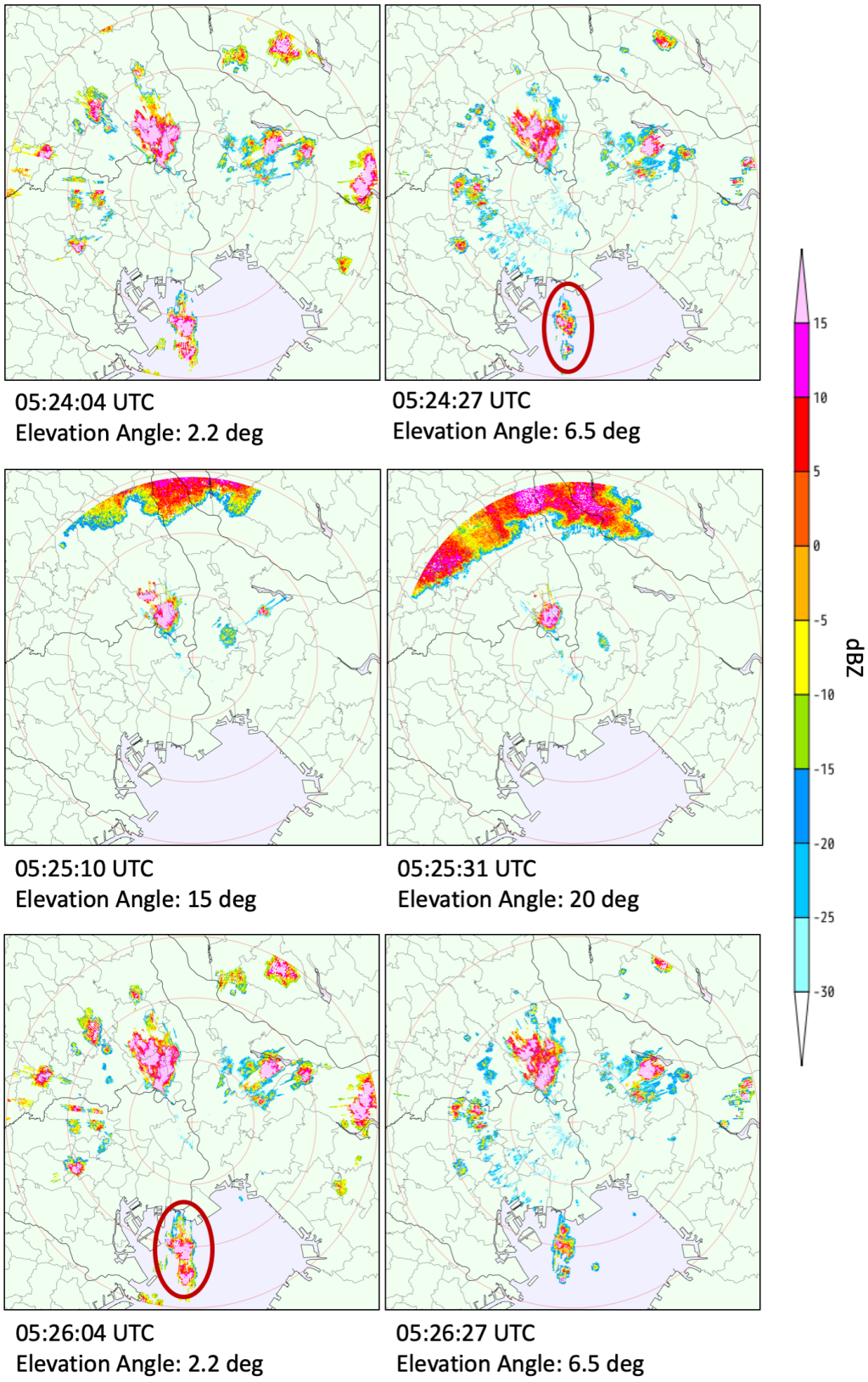

Figure 6.10 Ka-band radar at Edogawa Region at 6 different capture times. The red circle at capture times 05:24:27 UTC and 05:26:04 UTC indicates the target cloud under observation.

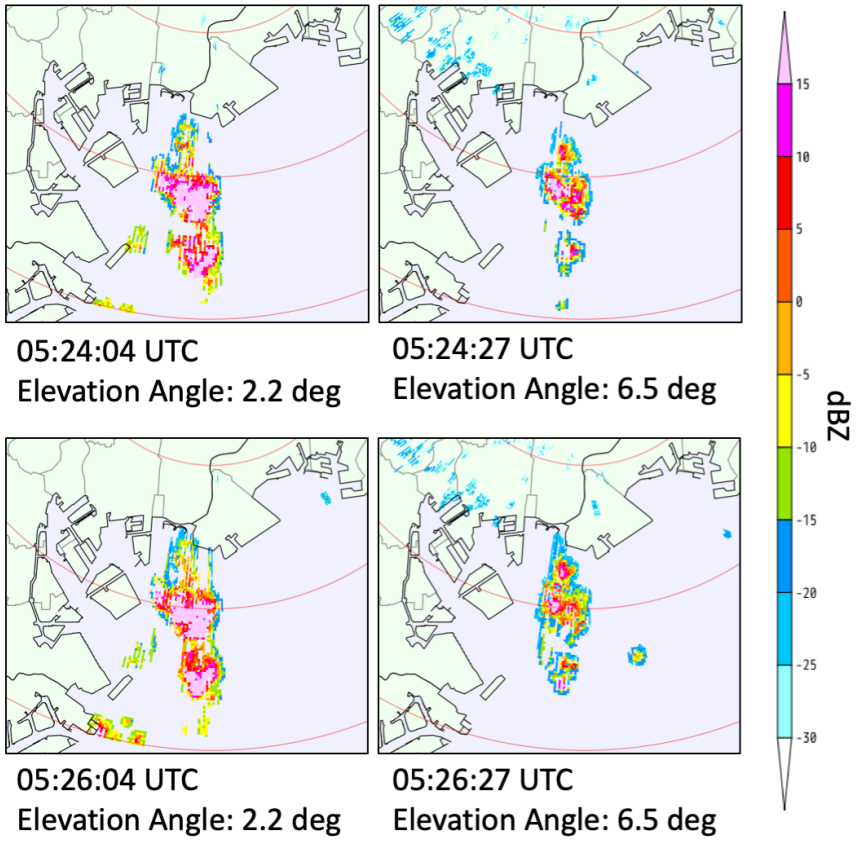

Figure 6.11 Ka-band radar measurement of August 14, 2019 isolated cumulonimbus cloud

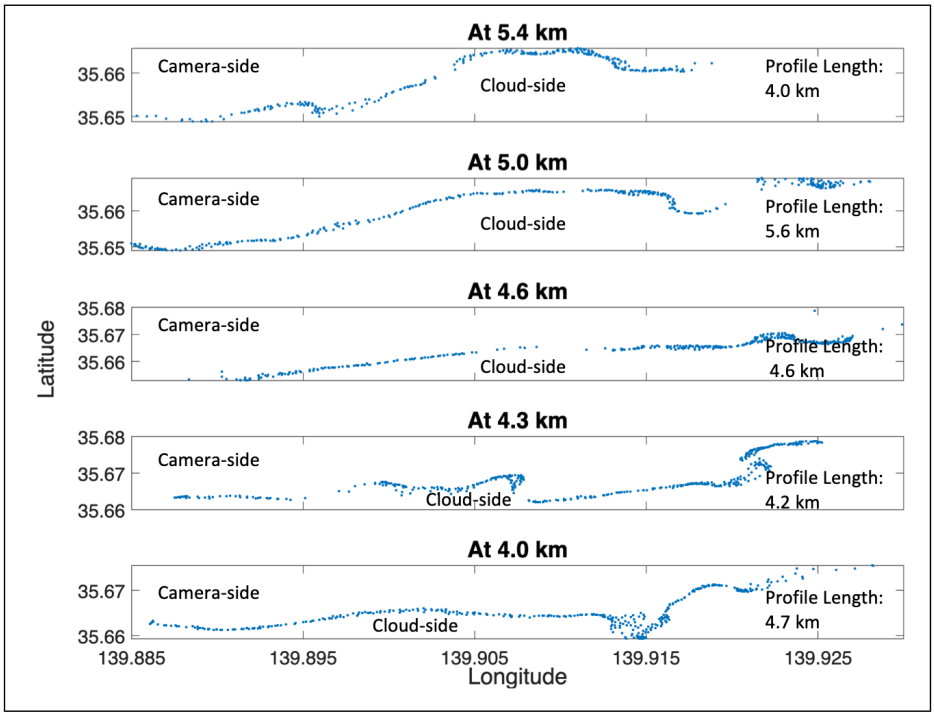

Figure 6.12 Cloud lateral cross-sections at different altitudes

6.3 Limitations

This approach is one of the few methods to use stereo-photogrammetry for cloud analysis. It still has room for improvement. For instance, it relies heavily on matched stereoscopic features between images, so resolution is important. Additionally, the algorithm used for the stereo-photogrammetry reconstruction is designed for structures with rigid features, such as buildings and ground feature points, thus, it has difficulty detecting faint cloud features. Finally, knowing the camera pose could help improve the accuracy of this technique.

Ground cameras have higher reprojection error relative to imaging sources that have elevation (satellites and aircraft images). Since this method is an opportunistic approach to stereo-photogrammetry, success rate is highly dependent on the location and the atmospheric conditions during the time of the observation. However, the advantages of ground observations should be utilized to the fullest by developing camera setups that will automatically capture cloud images for prolonged periods of time at higher elevations.

The output of this research is preliminary to estimating typhoon intensity and the output is not enough to observe typhoon development and its relationship to maximum wind speed and amount of precipitation. More field observations should be conducted in order to find the relationship of cloud-top altitude and cloud volume to typhoon intensity and precipitation rate.

Chapter 7

Conclusion

This chapter emphasizes the aims/objectives and the achievements of this research. It discusses the most significant results, as well as the limitations and suggestions for future studies.

7.1 Research Summary

Typhoons and torrential rains are weather phenomena that cause flooding and landslides, especially in the East and South-east Asian countries that are exposed to these extreme weather phenomena. In addition, the frequencies and intensities of typhoons and torrential rains are getting higher due to warming temperature. Because of this, measuring their intensity accurately can help mitigate the hazards that they bring. However, analysis of typhoon (size, shape of clouds and development rate) is difficult to perform because of its chaotic behavior and environmental factors that affect it. According to studies, the essential parameters for estimating typhoon intensity from remote sensing are cloud morphology, cloud-top height, and cloud profiling information across the center of the storm. For stronger typhoons, the typhoon eye and eyewall are also more prominent, making them good indicators of typhoon intensity. Typhoons and cumulonimbus clouds that could cause torrential rains have different spatial and temporal scales. This discrepancy in scaling makes it difficult to analyze clouds using a single imaging source. Thermal infrared from meteorological satellites that measures cloud altitude are unreliable because of inconsistent atmospheric temperatures. Furthermore, radar sensors have insufficient spatial and temporal resolution to measure small cloud particles. These show that the current methods have limitations.

In this research, a method was developed to analyze typhoons and isolated cumulonimbus clouds using stereo-photogrammetry from different imaging sources: satellite, aircraft, and cameras located on the ground. The cloud-top altitude was then estimated from stereo-photogrammetric models and validated using Himawari-8 TIR and dropsonde data.

For the satellite images, Diwata-2 captured multiple images of Typhoon Maysak, a Category 4 typhoon that hit Japan last September 2, 2020. We reconstructed a precise three-dimensional model of a typhoon using the monocular camera setup of the satellite. The area coverage of the model is approximately 33,100 km^2 with a ground resolution of 103 m and a 2.64 pix RMS reprojection. It has a latitude range of 31.1°N to 32.2°N

and longitude range of 126.1°E to 129.4°E. A maximum altitude of 16 km was estimated from the model which has an absolute difference of 1.2 km from the estimated cloud-top altitude using TIR. Although there are inconsistencies in the altitude profile between the two methods due to unknown camera rotations, the cloud structures observed are very similar.

For the aircraft reconnaissance, images of Typhoon Trami, a Category 5 typhoon that hit Japan last September 2018, was also captured using a monocular camera in the aircraft. Using stereo-photogrammetry, the first 3D model of a typhoon eye was reconstructed. The result of the stereo-photogrammetric model from the aircraft images has an area coverage of approximately 2,080 km^2 with a ground resolution of 6.08 m and a 2.37 pix projection error. The orthomosaic has a latitude range of 20.4°N to 20.9°N and a longitude range of 128.8°E to 129.6°E. The resulting altitude from stereo-photogrammetry shows that the cloud-top altitude of Typhoon Trami is approximately 14 km and has a huge overlap with the altitude estimate from TIR. The altitude profile from the stereo-photogrammetry has sufficient resolution to see the stair-step structure within the typhoon eye. This structure visualizes the eyewall replacement cycle of typhoons.

Multiple isolated cumulonimbus clouds were also modeled through stereo-photogrammetry of images from 5 ground cameras. The first ground observation was conducted at Edogawa City last August 14, 2019. Only 3 images were utilized for the reconstruction of the stereo-photogrammetric model. It has a resolution of 1.85m/pix with a 4.34 pix projection error and an area coverage of 151 km^2. The estimated cloud-top altitude from the model is 6.2 km which is higher than its TIR estimate of 3.7 km. Unlike all the other data, this observation was also detected by a radar located in Matsudo City which is 18 km away from the target cloud. The cloud height estimated from the radar ranges from 691m to 2.05 km. This shows that the stereo-photogrammetric model reconstructed from only 3 cameras could be erroneous as the scale and the position of the model's orthomosaic also has inconsistencies with the Himawari-8 image. However, due to low temporal resolution, it is difficult to measure the exact cloud height range of the target cloud using the ka-band radar. Based from the undetected cloud at elevation angle 10°, we can assume that its cloud-top altitude is lower than 3.20 km.

Another observation was conducted at the same location on September 5, 2020 and the resulting 3D model has an area coverage of 4.27 km^2 with a ground resolution of 1.85 m and a 3.2 pix projection error. The estimated cloud-top altitude is 3.4 km, 1.7 km higher than its TIR estimate.

From the results, our method shows significantly higher resolution than other imaging sources since most satellites and sensors have spatial resolution of 1 km at best, with the exception of Advanced Spaceborne Thermal Emission and Reflection Radiometer (ASTER) and Diwata-1. This enables the reconstruction of the stereo-photogrammetric model using our imaging sources. In addition, the stereo-photogrammetric model of the isolated cumulonimbus cloud shows the continuous cloud height range unlike the TIR which estimates just the cloud-top altitude.

For each model, cloud-top altitude was also estimated, and was compared with the cloud-top altitude estimated from Himawari thermal infrared (TIR) and dropsonde data. The altitude profiles of the models have good details of the cloud structures. However, cloud-top altitude can be improved when more images are used at higher resolution and with known camera rotation parameters. Furthermore, this study suggests the idea of analyzing clouds in volumetric perspective that could help improve the accuracy of extreme weather prediction in the future.

7.2 Future Work

In the research roadmap, the main objective is to predict the intensity of the typhoon and the precipitation rate of cumulonimbus clouds from cloud parameters (altitude and volume). To be able to do this, a preliminary approach for extracting the three-dimensional cloud structures using stereo-photogrammetry was developed and presented in this research. The 3D models were validated using other imaging sources, such as satellites, high-altitude cameras, and radar. However, to predict typhoon intensity and other torrential rain parameters from three-dimensional cloud structures, more observations should be done. Another way to utilize stereo-photogrammetry, is to observe how the cloud structures in typhoons and cumulonimbus clouds changes through time. This could help meteorologists understand how typhoons and cumulonimbus clouds develop and, eventually, dissipate.

Several improvements can be made to improve our stereo-photogrammetry technique:

i. Improve the 3D models by incorporating accurate camera pose into the three-dimension imaging software
ii. Develop camera setups that will automatically synchronize ground camera capture time
iii. Develop algorithm that can enhance image features and automatically detect delicate cloud features
iv. Synchronize ground camera capture with other sensors (Diwata-2, RISESAT, Mt. Fuji camera, radar data) for data comparison
v. Conduct more experiments to find the relationship of cloud volume to properties of torrential rain and to visualize typhoon development and eyewall replacement cycle
vi. Future studies could help validate the accuracy of this approach by using radar data

References

Butt, T. (2021, September 7). Retrieved from Here's Why Hurricanes are so Difficult to Predict: https://magicseaweed.com/news/heres-why-hurricanes-are-so-difficult-to-predict/11514/

Baking, A. (2016, March 18). Retrieved from https://acfc.asia/blogs/worlds-disaster-prone-cities-philippines/

Kossin, J., Knapp, K., Olander, T., & Velden, C. (n.d.). Global increase in major tropical cyclone exceedance probability over the past four decades. *Proceedings of the National Academy of Sciences 117 (22)*, (pp. 11975-11980).

Maskey, M., Ramachandran, R., Ramasubramanian, M., Gurung, I., Freitag, B., Kaulfus, A., . . . Miller, J. (2020). Deepti: Deep-Learning-Based Tropical Cyclone Intensity Estimation System. *IEEE Journal of Selected Topics in Applied Earth Observations and Remote Sensing*, 1-1. 10.1109/JSTARS.2020.3011907. .

Luo, Z., Stephens, G., Emanuel, K., Vane, D., Tourville, N., & Haynes, J. (2008). On the use of cloudsat and modis data for estimating hurricane intensity. *IEEE Geoscience Remote Sensing Letter*(5), 13–16 DOI: 10.1109/LGRS.2007.905341.

Dvorak, V. (1975). Tropical cyclone intensity analysis and forecasting from satellite imager. *Monthly Weather Review, 103*, 420–430,DOI: https://doi.org/10.1175/1520-0493(1975)103<0420:TCIAAF>2.0.CO;2.

Tsujino, S., Horinouchi, T., Tsukada, T., Kuo, H., Yamada, H., & Tsuboki, K. (2021). Inner-Core Wind Field in a Concentric Eyewall Replacement of Typhoon Trami (2018): A Quantitative Analysis Based on the Himawari-8 Satellit. *Journal of Geophysical Research: Atmospheres, 126*(7), DOI: 10.1029/2020jd034434.

Peduzzi, P., Chatenoux, B., Dao, H., De Bono, A., Herold, C., Kossin, J., . . . Nordbeck, O. (2012). Global trends in tropical cyclone risk. *Nature Climate Change, 2*(4), 289-294, DOI: 10.1038/nclimate1410.

Pun, I. F., Lin, I. I., & Lo, M. H. (2013). Recent increase in high tropical cyclone heat potential area in the Western North Pacific Ocean. *Geophysical Research Letters, 40*(17), 4680-4684, DOI: 10.1002/grl.50548.

Wu, C., Chou, K., Cheng, H., & Wang, Y. (2003). Eyewall Contraction, Breakdown and Reformation in a Landfalling Typhoon. *Geophysical Research Letters, 30*(17), DOI: 10.1029/2003gl017653.

Zhu, T., Zhang, D., & Weng, F. (2004). Numerical Simulation of Hurricane Bonnie (1998). Part I: Eyewall Evolution and Intensity Changes. *Monthly Weather Review, 132*(1), 225-241, DOI: 10.1175/1520-0493.

Hasler, A., Palaniappan, K., Kambhammetu, C., Black, P., Uhlhorn, E., & Chesters, D. (1998). High-Resolution Wind Fields within the Inner Core and Eye of a

Mature Tropical Cyclone from GOES 1-min Images. *Bulletin of the American Meteorological Society, 79*(11), 2483-2496, DOI: 10.1175/1520-0477.

Bell, M., & Montogomery, M. (2008). Observed Structure, Evolution, and Potential Intensity of Category 5 Hurricane Isabel (2003) from 12 to 14 September. *Monthly Weather Review, 136*(6), 2023-2046, DOI: 10.1175/2007mwr1858.1.

Liu, C., Liu, G., Lin , T., & Chao, C. (2010). Accumulated Rainfall Forecast of Typhoon Morakot (2009) in Taiwan Using Satellite Data. *Journal of the Meteorological Society of Japan. Ser. II, 88*(5), 785-798, DOI: 10.2151/jmsj.2010-501.

Dvorak , V. (1984). *Tropical cyclone intensity analysis using satellite data.* United States, National Environmental Satellite, Data, and Information Service.

Li, X., Zhang, J., Yang, X., Pichel, W., DeMaria, M., Long, D., & Li, Z. (2013). Tropical Cyclone Morphology from Spaceborne Synthetic Aperture Radar. *Bulletin of the American Meteorological Society, 94*(2), 215-230, DOI: 10.1175/bams-d-11-00211.1.

Wang, Y., & Wu, C. (2004). Current understanding of tropical cyclone structure and intensity changes ? a review. *Meteorology and Atmospheric Physics, 87*(4), 257-278, DOI: 10.1007/s00703-003-0055-6.

Yamada, H., Nasuno, T., Yanase, W., & Satoh, M. (2016). Role of the Vertical Structure of a Simulated Tropical Cyclone in Its Motion: A Case Study of Typhoon Fengshen (2008). *SOLA, 12*(0), 203-208, DOI: 10.2151/sola.2016-041.

Mack, R., Hasler, A., & Rodgers, E. (1983). Stereoscopic observations of hurricanes and tornadic thunderstorms from geosynchronous satellites. *Advances in Space Research, 2*(6), 143-151, DOI: 10.1016/0273-1177(82)90134-x.

Powell, M. (1990). Boundary Layer Structure and Dynamics in Outer Hurricane Rainbands. Part II: Downdraft Modification and Mixed Layer Recovery. *Monthly Weather Review, 118*(4), 918-938, DOI: https://doi.org/10.1175/1520-0493(1990)118<0918:BLSADI>2.0.CO;2.

Liu, K., & Chan, J. (1999, December 9). Size of Tropical Cyclones as Inferred from ERS-1 and ERS-2 Data. *Monthly Weather Review, 127*(12), 2992-3001, DOI: https://doi.org/10.1175/1520-0493(1999)127<2992:SOTCAI>2.0.CO;2.

Houze, R., Chen, S., Smull, B., Lee, W., & Bell, M. (2007). Hurricane Intensity and Eyewall Replacement. *Science, 315*(5816), 1235-1239, DOI: 10.1126/science.1135650.

Cheng, Y., Huang, S., Liu, A., Ho, C., & Kuo, N. (2012). Observation of typhoon eyes on the sea surface using multi-sensors. *Remote Sensing of Environment, 123*, 434-442, DOI: 10.1016/j.rse.2012.04.009.

Pan, Y., Liu, A., He, S., Yang, J., & He, M. (2013). Comparison of Typhoon Locations over Ocean Surface Observed by Various Satellite Sensors. *Remote Sensing, 5*(7), 3172-3189, DOI: 10.3390/rs5073172.

Jin, S., Wang, S., & Li, X. (2014). Typhoon eye extraction with an automatic SAR image segmentation method. *International Journal of Remote Sensing, 35*(11-12), 3978-3993, DOI: 10.1080/01431161.2014.916447.

Takashima, T., Takayama, Y., Matsuura, K., & Naito, K. (1982). Cloud height determination by satellite stereography. *Papers in Meteorology and Geophysics, 33*(2), 65-78, DOI: 10.2467/mripapers.33.65.

Seiz, G., Tjemkes, S., & Watts, P. (2007). Multiview Cloud-Top Height and Wind Retrieval with Photogrammetric Methods: Application to Meteosat-8 HRV Observations. *Journal of Applied Meteorology and Climatology, 46*(8), 1182-1195, DOI: 10.1175/jam2532.1.

Prata, A. (1997). Cloud-top height determination using ATSR data. *Remote Sensing of Environment, 59*(1), 1-13, DOI: 10.1016/s0034-4257(96)00071-5.

Naud, C., Mitchell, K., Muller, J., Clothiaux, E., Albert, P., Preusker, R., . . . Hogan, R. (2007). Comparison between ATSR-2 stereo, MOS O2-A band and ground-based cloud top heights. *International Journal of Remote Sensing, 28*(9), 1969-1987, DOI: 10.1080/01431160600641806.

Moroney, C., Davies, R., & Muller, J. (2002). Operational retrieval of cloud-top heights using MISR data. *IEEE Transactions on Geoscience and Remote Sensing, 40*(7), 1532-1540, DOI: 10.1109/tgrs.2002.801150.

Seiz, G., Davies, R., & Grun, A. (2006). Stereo cloud-top height retrieval with ASTER and MISR. *International Journal of Remote Sensing, 27*(9), 1839-1853, DOI: 10.1080/01431160500380703.

Castro, E., Ishida, T., Takahashi, Y., Kubota, H., Perez, G., & Marciano, J. (2020). Determination of Cloud-top Height through Three-dimensional Cloud Reconstruction using DIWATA-1 Data. *Scientific Reports, 10*(1), DOI: 10.1038/s41598-020-64274-z.

Department of Science and Technology - Advanced Science and Technology Institute. (2016). Retrieved from https://asti.dost.gov.ph/projects/ulat/

Tsuboki, K. (2017). Tropical cyclones-Pacific Asian Research Campaign for Improvement of Intensity estimations/forecasts (T-PARCII): A research plan of typhoon aircraft observations in Japan. *EGU General Assembly Conference Abstracts*, (p. 12847).

Ornauer, D. (2018, September 29). *Typhoon 28E (Trami), #53 FINAL*. Retrieved from Stars and Stripes: https://www.stripes.com/news/typhoon-28w-trami-53-final-1.548347

Ito, K., Yamada, H., Yamaguchi, M., Nakazawa, T., Nagahama, N., Shimizu, K., . . . Tsuboki, K. (2018). Analysis and Forecast Using Dropsonde Data from the Inner-Core Region of Tropical Cyclone Lan (2017) Obtained during the First Aircraft Missions of T-PARCII. *SOLA, 14*(0), 105-110, DOI: 10.2151/sola.2018-018.

Yamada, H., Ito, K., Tsuboki, K., Shinoda, T., Ohigashi, T., Yamaguchi, M., . . . Shimizu, K. (2021). The Double Warm-Core Structure of Typhoon Lan (2017) as Observed through the First Japanese Eyewall-Penetrating Aircraft Reconnaissance. *Journal of the Meteorological Society of Japan. Ser. II, 99*(5), 1297-1327, DOI: 10.2151/jmsj.2021-063.

Genkova, I., Seiz, G., Zuidema, P., Zhao, G., & Di Girolamo, L. (2007). Cloud top height comparisons from ASTER, MISR, and MODIS for trade wind cumuli. *Remote Sensing of Environment, 107*(1-2), 211-222, DOI: 10.1016/j.rse.2006.07.021.

Meteorological Satellite Center of Japan Meteorological Agency. (2021). *Meteorological Satellite Center of Japan Meteorological Agency*. Retrieved from Imager (AHI): https://www.data.jma.go.jp/mscweb/en/himawari89/space_segment/spsg_ahi.html

Stull, R. (2018). *Practical Meteorology: An Algebra-based Survey of Atmospheric Science.* Vancouver City, Canada: Sundog Publishing, LLC.

Bosisio, A., & Mallet, C. (1998). Influence of cloud temperature on brightness temperature and consequences for water retrieval. *Radio Science, 33*(4), 929-939, DOI: 10.1029/98rs00949.

Landolt, S., Bateman, R., & Bernstein, B. (2004). A Comparison of Satellite and Sounding Derived Cloud Top Temperatures . *20th Conf. on Weather Analysis and Forecasting/16th Conf. on Numerical Weather Prediction.* American Meteorological Society.

Iwabuchi, H., Putri, N., Saito, M., Tokoro, Y., Sekiguchi, M., Yang, P., & Baum, B. (2018). Cloud Property Retrieval from Multiband Infrared Measurements by Himawari-8. *Journal of the Meteorological Society of Japan. Ser. II, 96B*(0), 27-42, DOI: 10.2151/jmsj.2018-001.

Black, M., & Willoughby, H. (1992). The Concentric Eyewall Cycle of Hurricane Gilbert. *Monthly Weather Review, 120*(6), 947-957, DOI: 10.1175/1520-0493(1992)120<0947:tcecoh>2.0.co;2.

Palmen, E., & Newton, C. (1969). *Atmospheric Circulation Systems: Their Structure and Physical Interpretation.* London, UK: Academic Press.

Wallace, J., & Hobbs, P. (2006). *Atmospheric Science 2nd Edition: An Introductory Survey.* London, UK: Academic Press.

Agisoft Helpdesk Portal. (2020, September 16). *References List*. Retrieved from https://agisoft.freshdesk.com/support/solutions/articles/31000156964-references-list

Yoshida, K., Sakamoto, Y., Takahashi, Y., Kurihara, J., Yamakawa, H., & Takada, A. (2011). A Japanese Microsatellite Bus System for International Scientific Missions. *62nd International Astronautical Congress* (pp. Paper: IAC-11.B4.2.10). Cape Town, South Africa: Proceedings of IAC 2011.

Kuwahara, T., Yoshida, K., Sakamoto, Y., Kurihara, J., Takahashi, Y., Takada, A., & Yamakawa, H. (2012). Development Status of Microsatellite RISESAT, Hodoyoshi-2. *The 4th Nanosatellite Symposium (NSS)* (pp. URL: http://www.nanosat.jp/4th/pdf/Day3_1_S-3_01_Toshinori_Kuwahara/S-3_01_Toshinori_Kuwahara.pdf). Nagoya, Japan: Proceedings of the UN/Japan Workshop.

Kubo-oka, T., Kunimori, H., Fuse, T., Takenaka, H., Toyoshima, M., Kuwahara, T., . . . Takahashi, Y. (n.d.). *CDDIS NASA's Archive of Space Geodesy Data.* Retrieved from Collaboration of ranging and optical communication mission RISESAT: http://cddis.gsfc.nasa.gov/lw18/docs/papers/Posters/13-Po08-Kubooka.pdf

Bhatia, K., Vecchi, G., Knutson, T., Murakami, H., Kossin, J., Dixon, K., & Whitlock, C. (2019). Recent increases in tropical cyclone intensification rates. *Nature Communications, 10*(1), DOI: 10.1038/s41467-019-08471-z.

Lee, J., Im, J., Cha, D., Park, H., & Sim, S. (2019). Tropical Cyclone Intensity Estimation Using Multi-Dimensional Convolutional Neural Networks from Geostationary Satellite Data. *Remote Sensing, 12* (1), 108, DOI: 10.3390/rs12010108.

Schumacher, R. (2017, May 24). *Natural Hazard Science*. Retrieved from Heavy Rainfall and Flash Flooding:

https://oxfordre.com/naturalhazardscience/view/10.1093/acrefore/9780199389407.001.0001/acrefore-9780199389407-e-132

World Meteorological Organization. (2021). *World Meteorological Organization*. Retrieved from Tropical Cyclones: https://public.wmo.int/en/our-mandate/focus-areas/natural-hazards-and-disaster-risk-reduction/tropical-cyclones

Hayhoe, K., Wuebbles, D., Easterling, D., Fahey, D., Doherty, S., Kossin, J., . . . Wehner, M. (2018). *2018: Our Changing Climate. In Impacts, Risks, and Adaptation in the United States: Fourth National Climate Assessment* (Vol. 2). (L. Mearns, Ed.) Washington DC, USA: U.S. Global Change Research Program.

UP Media and Public Relations Office. (2018, October 26). *University of the Philippines*. Retrieved from Diwata-2, second PH microsatellite, set for launch: https://up.edu.ph/diwata-2-second-ph-microsatellite-set-for-launch/

Mainichi Japan. (2020, September 2). *The Mainichi: Japan's National Daily Since 1922*. Retrieved from Typhoon Maysak approaching southwestern Japan with strength: https://mainichi.jp/english/articles/20200902/p2a/00m/0na/002000c

JAXA. (2020, March 5). *JAXA Space Terchnology Dictorate I*. Retrieved from Challenges in Typhoon Track Predictions~ Typhoon KROSA (TY1910) in 2019: https://www.eorc.jaxa.jp/en/earthview/2020/tp200305.html

Kamogawa, M. (2020, March 20). *nippon.com*. Retrieved from The Mount Fuji Research Station: A Scientific Treasure Trove: https://www.nippon.com/en/japan-topics/g00822/the-mount-fuji-research-station-a-scientific-treasure-trove.html

Kubo-oka, T., Kunimori, H., Takenaka, H., Fuse, T., & Toyoshima, M. (2012). Optical Communication Experiment Using Very Small Optical TrAnsponder Component on a Small Satellite RISESAT. *International Conference on Space Optical Systems and Applications (ICSOS).* Ajaccio, Corsica, France: ICSOS 2012.

Hirschmuller, H. (2008). Stereo Processing by Semiglobal Matching and Mutual Information. *IEEE Transactions on Pattern Analysis and Machine Intelligence, 30*(2), 328-341, DOI: 10.1109/tpami.2007.1166.

National Oceanic & Atmospheric Administration. (2018, August). *Atlantic Oceanographic & Meteorological Laboratory.* Retrieved from Hector 2018 sondes: https://www.aoml.noaa.gov/hrd/Storm_pages/hector2018/sonde.html

Zehnder, J. (2021, August 26). *Encyclopedia Britannica*. Retrieved from tropical cyclone: https://www.britannica.com/science/tropical-cyclone

Haralick, R. (1980). Using perspective transformations in scene analysis. *Computer Graphics and Image Processing, 13*(3), 191-221, DOI: 10.1016/0146-664x(80)90046-5.

Posner, E. (2019, July 3). *Hearbeat*. Retrieved from ActiveStereoNet: The first deep learning solution for active stereo systems: https://heartbeat.comet.ml/activestereonet-the-first-deep-learning-solution-for-active-stereo-systems-f52ed2c6cd2

Agisoft LLC. (2021). Retrieved from Agisoft Metashape User Manual Professional Edition, Version 1.7: chrome-extension://efaidnbmnnnibpcajpcglclefindmkaj/viewer.html?pdfurl=https%3A%2F%2Fwww.agisoft.com%2Fpdf%2Fmetashape-pro_1_7_en.pdf&clen=2805189&chunk=true

Menzel, W. (2004, July). *University of Winconsin-Madison.* Retrieved from Applications with Meterorological Satellites: https://cimss.ssec.wisc.edu/rss/bertinoro/source/text/

Hasler, A., Strong, J., Woodward, R., & Pierce, H. (1991). Automatic Analysis of Stereoscopic Satellite Image Pairs for Determination of Cloud-Top Height and Structure. *Journal of Applied Meteorology, 30*(3), 257-281.

National Aeronautics and Space Administration (NASA). (2020, August 28). *Jet Propulsion Laboratory, California Institute of Technology*. Retrieved from Terra MISR Used to Visualize Cloud-top Heights From Tropical Storm Laura in 3D: https://www.jpl.nasa.gov/news/terra-misr-used-to-visualize-cloud-top-heights-from-tropical-storm-laura-in-3d

Maesaka, T. (2015). Cloud Radar Network in Tokyo Metropolitan Area for Early Detection of Cumulonimbus Generation . *37th Conference on Radar Meteorology.* Oklahoma, USA.